PETROLEUM RESEARCH JOURNAL

TECHNICAL PAPERS

ENGINEERING

Effect of strain rate and temperature on the susceptibility of 304 austenitic stainless steel to hydrogen embrittlement .....
F. El Shawesh 1

Effect of viscosity ratio on Archie saturation exponent .....
O.B. Al-Mahtot and W.E. Mason 7

Effect of porosity type upon Archie's parameters of carbonate reservoir .....
O.B. Al-Mahtot, W.E. Mason and M. Nasar 13

Simulation of new technique for measuring relative permeability and capillary pressure at capillary dominated flow .....
Mabruk A. Benrewin 17

Evaluation of clay and drilling fluid quality .....
Talal M. Mohammed and A.G. Alrabti 25

CHEMISTRY

A ^{14}C-Radiotracer study of the hydrogenation of ethyne on 0.3% $Pt/A1_2O_3$ (Europt-3).....
Ezziddin A. Arafa 31

Thermal stability study of Ras Lanuf jet fuel by NMR-spectroscopy and gas chromatography mass spectrometry.....
Gamil Alhakimi, Saleh Gebril, Ibrahim Rajab and Ibrahim Altijani 39

Determination of pollutants from heavy fuel oil (HFO) combustion in power plants ...
L.H. Ali, A.A. Ejabli and M.J. Gurbaj 45

SHORT COMMUNICATION

The Bahi Formation - its stratigraphic position, western Sirt Basin, Libya.....
Milad Ali Ghummed 57

VOLUME 10 - (1428) / (1998)

Petroleum Research Centre
P.O. Box 6431, Tripoli
Great Socialist People's Libyan Arab Jamahiriya

Petroleum Res. J. Vol. 10 (1998); P. 1-6, 7 Figs.

Effect of Strain Rate and Temperature on the Susceptibility of 304 Austenitic Stainless Steel to Hydrogen Embrittlement

F. El Shawesh*

أثر الحرارة ومعدل الانفعال على قابلية الفولاذ المقاوم للتآكل نوع 304 للتصدع الهيدروجيني

فوزي الشاوش

عدد من عينات الشدّ المصنوعة من الفولاذ المقاوم للتآكل نوع 304 شحنت بالهيدروجين كهروكيميائياً في وسط مائي يحتوي على 1 عياري حمض الكبريتيك مضافاً إليه قليل من زرنيخ الصوديوم أثناء تعرضها لمعدلات إنفعال عند درجة حرارة الغرفة (22±2C°) وأخرى عالية (70±2C°). نتائج إختبارات الشد عند درجة حرارة الغرفة بيّنت حدوث إنخفاض كبير في لدونة الصلب عند معدلات إنفعال بطيئة، كما أن الفحص المجهري لأسطح الكسور لعينات الشد (Fracture Morphology) أوضح بأنها هشة وأن إنتشارها كان بين وعبر حبيبات الصلب.

عندما شحنت عينات الشد عند درجة حرارة عالية (70±2C°) حدث إنخفاض كبير في قابلية الصلب للتصدع الهيدروجيني حيث أن عينات الشد كانت لها لدونة أعلى من التي كانت لعينات الشد التي تم إختبارها عند درجة حرارة الغرفة، كما أن نسبة اللدونة بها تزداد بزيادة معدلات الانفعال. أوضح الفحص المجهري لأسطح الكسور بأنها شبه هشة وأن نسبة اللدونة بها تزداد عند معدلات الإنفعال السريعة والبطيئة جداً.

بصفة عامة نتائج إختبار الشد أكدت بأن قابلية الصلب المقاوم للتآكل للتصدع الهيدروجيني تعتمد كلياً على درجة الحرارة ومعدل الإنفعال (strain rate).

Abstract: *Cathodic charging of notched 304 austenitic stainless steel specimens was carried out in aqueous solution of 1N H_2SO_4 containing 250 mg/l $NaAsO_2$ at room temperature and 70±2°C while undergoing tensile strain over a wide range of crosshead speeds of 833 µm/s, 83 µm/s, 8.3 µm/s, 833 nm/s, 83 nm/s and 9.8 nm/s.*

Test at room temperature 22±2°C resulted in a marked reduction in the elongation to fracture ratio (Esol/Eair) with reduction of the crosshead speed. However, little reduction was observed for stress to fracture ratio (σsol/σair). Cleavage and intergranular where the predominant fracture mode when tests were carried out at a low crosshead speed. The extent of these modes of fracture was observed to increase with reducing of crosshead speed.

Cathodic charging of 304 austenitic stainless steel at 70±2°C caused less reduction in the elongation to fracture ratio compared to the tests carried out at room temperature. Consistent with the room temperature test results, the reduction in the elongation to fracture ratio was found to increase with reduction of the crosshead speed. However, restoration in the elongation to fracture ratio was exhibited by 304 austenitic stainless steel specimens tested at the lowest crosshead speed of 9.8 nm/s. These results are in good

*Petroleum Research Centre, P.O. Box 6431, Tripoli, Libya

agreement with the finding that the hydrogen embrittlement is temperature and strain dependent.

Cleavage fracture associated with the plastic deformation was the predominant fracture mode exhibited by 304 austenitic stainless steel specimens tested at 70±2°C over low crosshead speed.

INTRODUCTION

Austenitic stainless steels were observed to have good resistance to hydrogen embrittlement and, therefore, they were frequently chosen as the suitable material in environments containing hydrogen. However, a number of studies have shown that austenitic stainless steels are susceptible to hydrogen embrittlement, though not to the extent of ferritic stainless steels. This owing to the differences in the solubilities and-diffusivities of hydrogen within these two alloys.[1]

For austenitic stainless steels, it has been established that the degree of embrittlement in tensile tests increases as the time of hydrogen charging increases and is dependent on strain rate and temperature[1]. The most severe embrittlement was observed to occur at low strain rates and at temperatures below or at room temperature[2]. Despite many previous studies on hydrogen assisted cracking in austenitic stainless steel, there are no reliable, consistent or uniform data about the the effect of hydrogen on the mechanical properties as functions of strain rate and temperature.

In the current work, specimens of 304 austenitic stainless steel were cathodically charged at current density of 0.4 mA/cm^2 in aqueous solution of 1N H_2SO_4 containing $NaAsO_2$ at room temperature and 70±2°C while undergoing tensile strain over a wide range of crosshead speeds. The effect of hydrogen on the mechanical properties (ductility and strength) and change of the fracture morphology for 304 austenitic stainless steel as function of temperature and strain rate (crosshead speed) will be presented and discussed.

EXPERIMENT

A commercial 304 austenitic stainless steel specimens with the required dimension was machined from 0.8 mm thick sheet supplied in the annealed condition. A 60°V notch were machined at the middle of all tested specimens in order to promote the initiation and propagation of single crack to enable convenient investigation of the tested specimens (Fig.1). In order to remove the stresses induced during specimens preparation, all machined specimens were given solution treatment at 1050°C for 1 hour. The chemical composition of the received sheet is shown in Table 1.

Table 1. Chemical composition (wt%) of 304 austenitic stainless steel specimen used throughout the work.

Materials	C	Mn	Si	P	S	Cr	Ni
304 S.S	0.04	1.42	0.32	0.024	0.002	18.36	8.73

The all tested specimens were cathodically charged at a current density of 0.4 mA/cm^2 in aqueous solution of 1N H_2SO_4 containing $NaAsO_2$ while undergoing tensile strain over a wide range of crosshead speeds of 833 μm/s, 83 μm/s, 8.3 μm/s, 833 nm/s, 83 nm/s and 9.8 nm/s at room temperature and 70±2°C. For comparison, the same number of specimens were tested in air at room temperature and 70±2°C (in oil). The degree of embrittlement for 304 austenitic stainless steel was evaluated by dividing the value of elongation {Esol} and stress {σsol} to fracture in solution over the elongation{Eair}and stress{σair} to fracture in air at eash used crosshead speed. The obtained values of Esol/Eair and σsol/σair are plotted versus the all-used crosshead speeds.

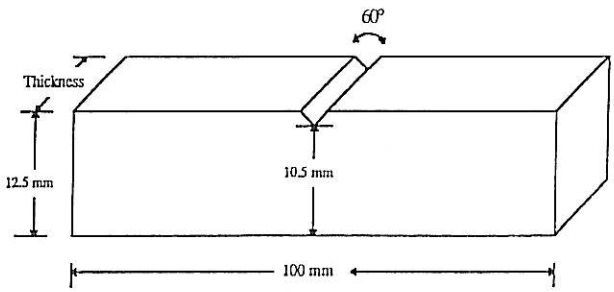


Fig. 1. Schematic representation showing the shape and dimensions (mm) of the type of specimen used in the hydrogen embrittlement test.

The resulted fracture surfaces were cleaned in acetone using ultrasonic and then dried. A scanning electron microscope (SEM) was then

used to examine the changes in the fracture morphology as a result of hydrogen embrittlement.

RESULTS AND DISCUSSION

Mechanical Properties (ductility)

The results of elongation to fracture ratio for 304 austenitic stainless steel specimens tested at room temperature and 70±2°C are shown in Figure 2 as a function of crosshead speed. It can be observed that 304 austenitic stainless steel specimens is susceptible to hydrogen embrittlement when tested at room temperature and 70±2°C over low crosshead speeds. Testing at 70±2°C markedly reduce the susceptibility of 304 austenitic stainless steel to hydrogen embrittlement. However, little restoration in the embrittlement was observed when the test was carried out at 70±2°C over the lowest used crosshead speed of 83 nm/s (Fig. 2).

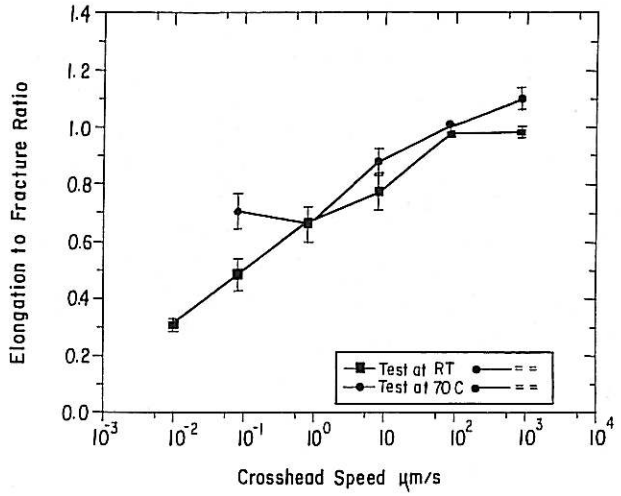


Fig. 2. Relationship between the elongation to fracture ratio and the crosshead speed for 304 austenitic stainless steel specimens fractured at room temperature and 70±2°C in aqueous solution of 1N H_2SO_4 containing $NaAsO_2$.

The results of stress to fracture ratio for 304 austenitic stainless steel specimens tested at room temperature and 70±2°C are shown in Figure 3. Consistent with the elongation ratio results, the stress ratio was observed to decrease with reduction in the crosshead speed. Since the resulting elongation ratio was observed to be more sensitive to hydrogen embrittlement than the stress ratio, during the discussion, the emphasis will be placed on the elongation to fracture ratio.

The reduction in the elongation to fracture ratio with lowering of crosshead speeds is consistent with the finding that the straining at slow crosshead speeds enhances the formation of high localized hydrogen concentration which are required to cause severe embrittlement[3,4]. The high potential sites for hydrogen concentration are dislocations, grain boundaries, and inclusions. Therefore, during straining high amounts of hydrogen is expected to be interacted or carried out by the mobile dislocations at the crack tip. These mobile dislocations are expected to tangle or pile up against any obstacles (*e.g* inclusions and grain boundaries) encountered its movement. Therefore, high hydrogen concentration, well in excess of the equilibrium content, can develop leading to severe embrittlement[3,5,6].

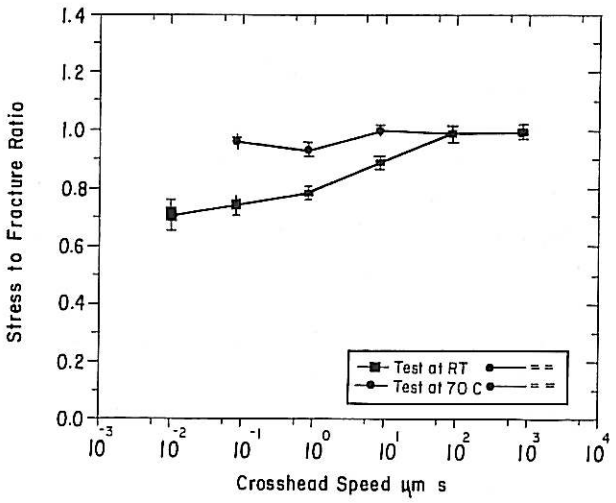


Fig. 3. Relationship between the stress to fracture ratio and the crosshead speed for 304 austenitic stainless steel specimens fractured at room temperature and 70±2°C in aqueous solution of 1NH_2SO_4 containing $NaAsO_2$.

When the test was carried out at 70±2°C, marked reduction in the susceptibility of 304 austenitic stainless steel to hydrogen embrittlement was observed. This can be attributed to the reduction in the localized hydrogen concentration in the test specimens when the test was carried out at 70±2°C[7,8]. As stated above, if the hydrogen embrittlement by dislocation is assumed to be vital to the hydrogen embrittlement mechanism, the hydrogen concentration on the mobile dislocations is thought to be low due to enhanced diffusion of hydrogen with increases in temperature[7,8]. In other words,

increase in temperature results in destabilization of hydrogen laden with dislocation and homogenize its very rapid[3]. This, in turn, results in a low hydrogen concentration at potential sites such as inclusions and dislocations. at which dislocation pile-ups takes place Hence, less embrittlement is attained. High localized hydrogen concentration is required in order to cause severe embrittlement[3].

Louthan *et al.*,[3] have demonstrated the effect of temperature on the susceptibility to the hydrogen embrittlement as follows.

The amount of hydrogen transported (C_T) for any given amount of dislocation motion is dependent on $C_\perp$ through the following equation[3].

$$C_T \alpha \sigma_m C_\perp V b L \text{ ———————— } (1)$$

Where C_T is the amount of hydrogen transported and ?m is the density of the mobile dislocation which have a hydrogen atmosphere and a burger vector, b. These dislocation are assumed to move with an average velocity of V, through an average distance L. Increasing the temperature tends to decrease the ratio of the hydrogen concentration on the dislocation core $C_\perp$ with respect to the lattice hydrogen concentration C_L. The relationship between the lattice hydrogen concentration of the dislocations is as follows[3].

$$C\perp = C_L \exp(-G_B / RT) \text{ ———————— } (2)$$

Where G_B is the binding energy between the hydrogen and the dislocation.

The restoration in elongation reduction may be attributed to the diffusion-out of hydrogen from the mobile dislocations at the lowest used crosshead speed of 83 nm/s. This is obviously due to the faster diffusivity of hydrogen from dislocations compared with dislocation velocity. Therefore, little amounts of hydrogen are expected to be dumped at obstacles at which dislocations piled-up, hence, less embrittlement resulted. As stated above, high localized hydrogen is required in order to embrittle the 304 austenitic stainless steel[3].

FRACTOGRAPHY

The effect of hydrogen, strain rate and temperature on the changes of fracture morphology of 304 austenitic stainless steel was studied and the results can be given as follows. Generally four features were observed on the fracture surfaces of tested specimens. The all air tested specimens at room temperature and 70±2°C (oil) exhibited ductile fracture as shown in Figure 4. Marked change in the fracture morphology was observed when 304 specimens tested at room temperature over low crosshead speeds of 83 nm/s and 9.8 nm/s. Cleavage and faceted intergranular fracture were the predominant fracture modes (Fig. 5). As the crosshead speed was increased above 83 nm/s, the percentage of ductile fracture to brittle fracture (cleavage) starts to increase (Fig. 6), for specimen tested at crosshead speed of 833 nm/s.

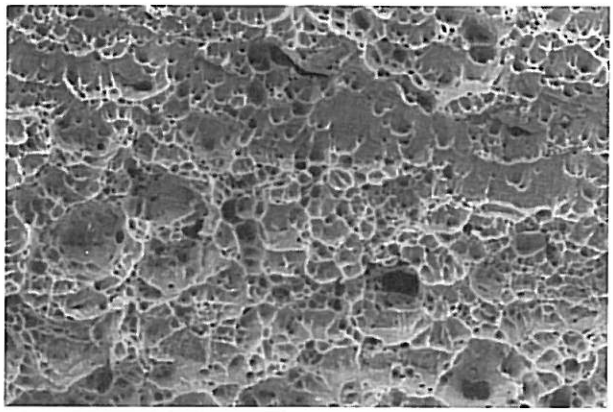


Fig. 4. Typical appearance of S.E.M. fractograph for a 304 austenitic stainless steel specimen strained in air over a wide range of crosshead speeds.

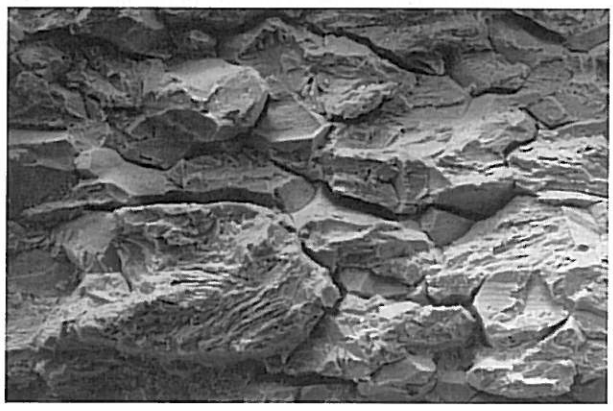


Fig. 5. S.E.M. fractograph of a 304 austenitic stainless steel specimen strained in solution at a crosshead speed of 9.8 nm/s. Fractograph shows both cleavage and faceted intergranular fracture.

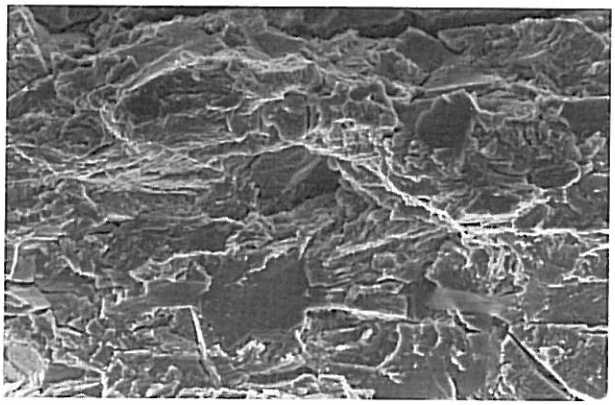


Fig. 6. S.E.M. fractograph for a 304 austenitic stainless steel specimen strained in solution at a crosshead speed of 833 nm/s. Fractograph shows that cleavage fracture is predominant. Little plastic deformation is visible.

The results of fracture morphology are consistent with the elongation ratio results when the test was carried out at 70±2°C. At a low crosshead speed of 83 nm/s, cleavage or quasi-cleavage like fractures were predominant (Fig.7) while above it, the percentage of ductile fracture to quasi cleavage fractures increases.

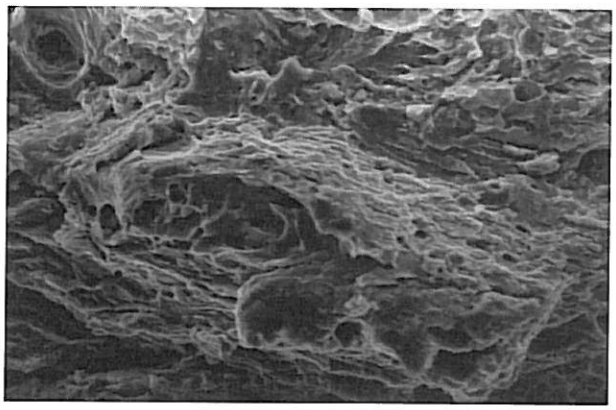


Fig. 7. S.E.M. fractograph for a 304 austenitic stainless steel specimen strained in solution at 70±2°C at the lowest crosshead speed of 83 nm/s. Fractograph shows quasi-cleavage fracture associated with some plastic deformation.

The observation of cleavage and intergranular fractures at the lowest crosshead speeds of 83 nm/s and 9.8 nm/s may be attributed to the high localized hydrogen concentration in the test specimens[3,9]. This may be owing to the pile-ups of mobile dislocations saturated with hydrogen against the obstacles (e.g inclusions, grain boundaries etc..) at the strained crack tip(3,9(. As stated above, high hydrogen conentration are required in order to embrittle the 304 austenitic stainless steel[3]. Increases of crosshead speed increase the percentage of ductile to cleavage fractures. This is mainly due to formation of low hydrogen concentration when the test was carried out at a high crosshead speed[4].

Cleavage fracture had been observed by many workers[10,11]. However, mixed mode, cleavage and faceted intergranular fracture of annealed 304 austenitic stainless steel, as observed in the current work, has not been previously shown.

Hydrogen charging at 70±2°C reduce the percentage of the ductile fracture with respect to the cleavage fracture owing to the low localized hydrogen concentration in the test specimens[3,5]. Generally tested at a temperature higher than room temperature, resulted in homogenization of hydrogen concentrated at obstacles present at crack tip such as dislocations and inclusion[3]. Therefore, low hydrogen concentration is attained, hence, less embrittlement was resulted.

CONCLUSIONS

1- The 304 austenitic stainless steel is significantly susceptible to hydrogen embrittlement when tested at room temperature over low crosshead speeds of 83 nm/s and 9.8 nm/s.

2- Marked decrease in the susceptibility of 304 austenitic stainless steel to hydrogen embrittlement was observed when the test was carried out at 70±2°C over the all-used crosshead speeds.

3- Transgranular and cleavage types of fracture modes were observed when 304 austenitic stainless steel was tested at room temperature over low crosshead speeds of 83 nm/s and 9.8 nm/s.

4- Transgranular cleavage, associated with plastic deformation, was the predominant fracture when 304 austenitic stainless steel was tested at 70±2°C over low crosshead speed of 83 nm/s.

5- The susceptibility of 304 austenitic stainless steel to hydrogen embrittlement was observed to decrease with the increase of test temperature and decrease of crosshead speed.

REFERENCES

[1] Whiteman, M. B. and Troiano, R. A.,1965, Corrosion, **21**, p.53.

[2] Holzworth, M. L., 1969, Corrosion, **22**, p.107.

[3] Louthan, M. R.1974, Hydrogen in Metals, (I. M. Bernstein and A. W. Thompson eds.), ASM, Metal Park, Ohio, p.53.

[4] Johnson, H. H. and Troiano, A. R., 1957, Nature, **179**, p. 777.

[5] Louthan, M. R., Caskey, G. R., Donovan, J. A. and Rawl, P. E., 1972, *Mater. SC:. Eng.*, 10, p.357.

[6] Thompson, A. W., 1974, *Hydrogen in Metals*, (I. M. Bernstein and A. W. Thompson eds.), p. 91, *ASM*, Cleveland, p. 91.

[7] Tien, J. K., Thompson, A.W., Bernstein, I. M. and Richards, R. W., 1976 *Metall. Trans.*, **7A**, p.821.

[8] Tien, J. K., 1976, *Effect of Hydrogen on Behavior of Materials*, (A. W. Thompson and I. M. Bernstein eds.), TMS-AIME, p. 304.

[9] West, A. J. and Louthan, M. R., 1979, *Metall Trans.* **10A**, p. 1675.

[10] Eliezer, D. E. Chakkrapani, D. G., Altstetter, L. J. and Pugh, E. N., 1979, *Metall Trans.*, **10A**, p. 935.

[11] Hanninen, H. and Hakkarainen, T., 1979, *Metall Trans.*, 10A, p. 1196.

Petroleum Res. J. Vol. 10 (1998); P. 7-11, 5 Figs.

Effect of Viscosity Ratio on Archie Saturation Exponent

O.B. Al Mahtot* and W.E. Mason*

تأثير نسبة اللزوجة على مُعامل التشبع المائي للصخور

عمران المحتوت و و.ي. ميسن

إن قياس معامل التشبع المائي للصخور بواسطة تسجيلات مقاومة التيار الكهربائي يعتمد على قياس معامل المقاومة الكهربائية والذي يحدد معملياً على عينات لبية باستخدام معادلة Archie.

أي خطأ في قياسات معامل التشبع المائي سوف ينتج عنه خطأ كبير في تقديم الاحتياطي النفطي في المكامن النفطية. معادلة Archie تفترض أن معامل التشبع المائي يتغير تبعاً لتغير معامل مقاومة التيار الكهربائي في الصخور ولا تأخذ في الاعتبار تغيير الخواص الطبيعية لسوائل المكامن النفطية.

إزداد في الأونة الأخيرة إستعمال طريقة الحقن المستمر في الصناعة النفطية حيث يتم وبصفة مستمرة إحلال المياه المالحة محل النفط الخام تحت نسبة لزوجة ثابتة. في هذه الدراسة تم تقديم طريقة معملية لقياس معامل مقاومة التيار الكهربائي في الصخور باستخدام عدة نسب للزوجة سوائل الإزاحة والسوائل المكمنية المزاحة، حيث أن جميع الطرق القديمة تستخدم نسبة لزوجة ثابتة. كما تم دراسة تأثير تغيير نسب اللزوجة على تغيير معامل التشبع المائي في المكامن النفطية.

تم إجراء التجارب المعملية على عدد أربع عينات صخرية ذات نسب لزوجة عالية ومنخفضة. أثبتت نتائج هذه التجارب أن تغيير نسبة اللزوجة أثّر تأثيراً كبيراً على شكل تنمى العلاقة بين معامل التشبع المائي ومعامل مقاومة التيار الكهربائي في الصخور، حيث يمكن ملاحظة ذلك في المنحنيات المتضمنة لهذه الدراسة، كما لوحظ أن خواص السوائل المكمنية وكذلك سوائل الإزاحة مهمة جداً عند إجراء التجارب المعملية لحساب معامل التشبع المائي للصخور، وتعتبر لزوجة هذه السوائل من أهم هذه الصفات.

Abstract: *Water saturation determination from wireline resistivity log data depends on measurement of the resistivity index on core samples. Resistivity index measurements carried out in the laboratory are the input to the second Archie equation; $I=Rt.Ro\text{-}Sw^{-n}$. Errors in the evaluation of the saturation exponent (n) can give rise to serious errors in the estimation of hydrocarbon saturations. This equation assumes that the same value of water saturation should give the same value of resistivity whatever the fluids characteristics used, because Sw and Rt are the only variables in the equation. It is assumed that this equation is independent of the fluids characteristics.*

The continuous injection technique is used increasingly in the oil industry. In this technique, one fluid phase (brine) is continuously displaced by another (oil) at a fixed viscosity (Brine/Oil) ratio. An experimental approach is proposed here in which repeated resistivity index measurements are carried out on the same core samples at different viscosity ratios. The effect of viscosity ratio on the saturation exponent for the core sample can then be investigated. Four carbonate samples with a wide range of porosity and permeability were tested to demonstrate resistivity index measurements at low and high viscosity ratios. The results showed that the fluid characteristics, such as viscosity ratio, have a crucial effect on the I versus Sw relationship. For some of the viscosity ratio used, the second Archie

*The Robert Gordon University, Aberdeen, U.K.

equation consists of two straight-line segments on a log-log; this may be due to a bimodal pore size distribution in the core samples used or due to the influence of other factors. Use of the continuous injection technique at different viscosity ratios has demonstrated that for water-wet samples, a different I versus Sw correlation can be obtained. It is, therefore, recommended that for resistivity index measurements, fluids characteristics represent the reservoir of interset should be used in order to obtain a reliable I versus Sw relation and, hence, an appropriate value of saturation exponent.

INTRODUCTION

Water saturation is commonly determined from electric well logs based on the second Archie equation[1]: $I=Sw^{-n}=Rt/Ro$. The Archie's parameters are usually obtained from laboratory measurements on core samples. It is assumed in laboratory measurements, that the saturation is distributed uniformly throughout the sample and that the saturation exponent n is constant over the saturation range. However, many cases are encountered where the resistivity index (I) shows a non-linear relationship with the brine saturation (Sw). Wettability, microporosity and capillary end effects are the main factors which contribute to this nonlinearity.

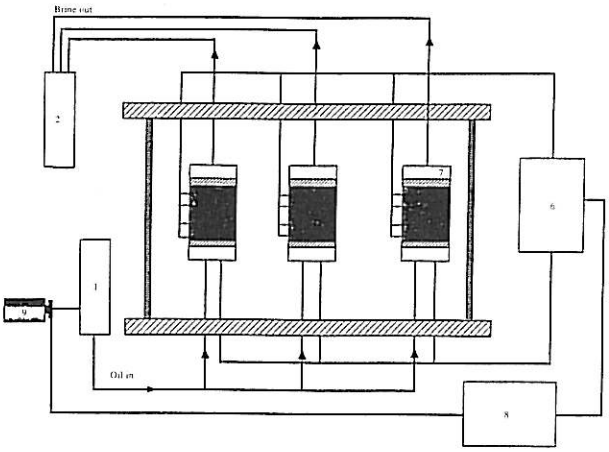
Archie's equation assumes that the same value of water saturation should give the same value of resistivity, whatever the fluid characteristics used, because Sw and Rt are the only variable in the equation. It is also assumed that this equation is independent of the fluids characteristics. The experimental conditions, and especially the viscosity ratio for the continuous injection technique, have an important influence on the I versus Sw curves. If inappropriate oil and brine viscosities are used in resistivity index measurements, an erroneous value of saturation exponent may be obtained. The influence of viscosity ratio on I versus Sw relationships has received little attention in the past, probably because of the time and cost involved in such experiments. However, unreliable values of saturation exponent can result in large errors in hydrocarbon determination[2]. Generally, the fluid distribution in porous media is function of rock type, pore structure characteristics, wettability, fluid properties, stress, rate of injection of displacing fluid and desaturation history. The pore structure also effects the profile of the displacing fluid front which, in turn, modifies the fluid distribution behind it and, hence, the resistivity values[3].

A number of different techniques have been devised to measure the electrical resistivity of rocks partially saturated with brine. The porous plate method, the centrifuge method and the continuous injection method are the techniques currently used in the oil industry. Of these, the most recently developed is the continuous injection method which is powerful, accurate, rapid and provides a continuous curve of I versus Sw rather than a limited number of points[2]. In this technique, oil is injected in order to displace brine at a fixed viscosity ratio. This method has the advantage that experimental error can be minimized by automation of the measurement procedure and measurements can be performed at effective reservoir stress. In this paper, an experimental approach is proposed in which repeated resistivity index measurements are carried out on the same samples at different viscosity ratios.

EXPERIMENTAL PROCEDURE

Low and high viscosity ratio experiments were carried out on selected carbonate samples and the viscosity ratio chosen were respectively 0.1 and 0.6. Figure 1 shows the layout of the apparatus used and Figure 2 illustrates the viton core sleeve with multiple electrode system. The samples, fully saturated with brine of concentration 100 g/l, were then mounted in a multiple core holder made of aluminum and subjected to an initial confining pressure of 400 psi, which was subsequently increased to 3000 psi. The sample pore volume was calculated based on the brine volume collected in pipettes attached to the outlet of each sample. The system was allowed to come to equilibrium and oil was then injected at one end of the sample and brine was expelled at the other end through a semipermeable membrane used to prevent passage of the oil at the outlet of the sample. The semipermeable membrane was supported on a brine saturated high porosity glass disc. Voltage, phase angle and temperature were monitored continuously during the oil injection process. All samples were previously made preferentially water-wet by first cleaning with methanol, then firing to 600°C for one day in a high temperature furnace[4]. Before the desaturation process began and the samples loaded, the resistivity of fully

saturated samples (Ro) were measured. The oil/ brine desaturation process was then started and *I* was measured when both capillary and electrical equilibrium was reached at the confining stress used. This equilibrium was indicated when there was no further change in resistance (*i.e.* no further fluid redistribution along the core length).

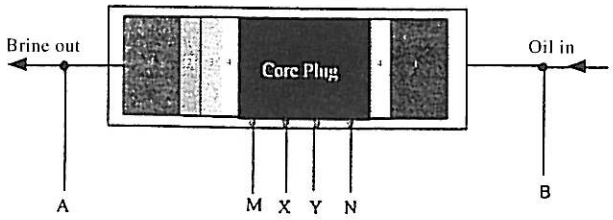


1 – Oil supply
2 – Brine volume measurement
3 – Pressure vessel
4 – Potential electrodes
5 – Rock samples
6 – Resistivity box
7 – Capillary diaphragm
8 – Computer cell
9 – Displacement pump

Fig. 1. Schematic diagram of core holder and resistivity index measurement apparatus.

The average core saturation was calculated volumetrically be deducting the volume of brine displaced from the pore volume. Oil was injected at the low rate. A displacement pump equipped with a piston was connected to the core holder. The amount of displaced fluid was measured by a calibrated potentiometer connected to the pump piston. The pump was regularly calibrated for the experimental conditions. The samples were subjected to the re-cleaning process to remove oil contamination and to keep them in water-wet condition throughout the experiment. The resistance of the samples was measured at 1kHz to minimize polarization effects[5]. The resistivity values were corrected for slight temperature variations by using Arp's equation[6].

To begin the continuous injection process, the displacement pump was started to inject the oil into the core holder. The first three samples, saturated with brine (μo = 2 cp) desaturation process was started, and the resistivity index *I* was



1 – Core holder end
2 – Semi-permeable membrane
3 – Ceramic disk
4 – Filter papers
A.B. – Current electrodes
M.X.N.Y. – Potential electrodes

Fig. 2. Schematic diagram of core sleeve with multi electrodes system.

measured when the capillary and electrical equilibrium was reached. This equilibrium was indicated when there was no further change in resistivity. The average core saturation was calculated volumetrically by deducting the volume of brine displaced from the pore volume. After, the resistivity index measurements were accomplished for the three samples at a low viscosity ratio. The samples were then unloaded and subjected to recleaning and then reloaded for the next measurements at a high viscosity ration (μw=1.2 cp and μo=2 cp).

DISCUSSION

The viscosity ration (μ_R), defined here as a ratio of displaced (Brine) fluid viscosity to the displacing fluid (oil) viscosity. High (μ_R=0.1) ratio was used. The fluid flows through a porous media (core or reservoir) is affected by the interaction of the local pore structure with viscous, capillary and gravitational forces[7]. The displacement of water by oil in a porous media is not a simple process and does depend on many factors such as the physical properties of the fluids. The flow mechanism, during the displacement, affects the fluids distribution and influences the resistivity index value. A transition zone exists since first oil starts to displace brine and this zone travels along the core sample until the end. The zone has different shapes depending on the pore structure and the forces controlling it. Whenever this transition zone passes through and has a short length while it progresses, the front can be named as flat front, and small clusters will be left behind. When this zone has a longer length, it can be considered as a fingering front. The second type

of front usually leaves larger clusters behind it than the first type. These large clusters would cause non-uniform saturation distribution and curved *I* versus Sw relationship would be obtained. The viscous force is one of many factors which controls and forms the shape of the front and, subsequently, different *I* versus Sw relationships are obtained at different viscosity ratios. Figures 3, 4 and 5 represent *I*/Sw plots for all the tested samples at two viscosity ratios. At a lower ratio, the *I* versus Sw relation is more uniform than at the higher ratio. Also, the desaturation process at low μ_R covers much Sw range than at a high ratio. This can be attributed to the fact that a thin water film is left behind when lower μ_R is used, while a thicker film of water is left behind at a higeher ratio. However, water was produced in case of high μ_R even after oil reached the sample end. It can be considered that a uniform saturation distribution was obtained for the sample at low μ_R. The high viscosity ratio experiments produced n values lower than those at a low ratio and the difference in n values reached about 0.7 and, subsequently, yielded a 12% error in Sw value.

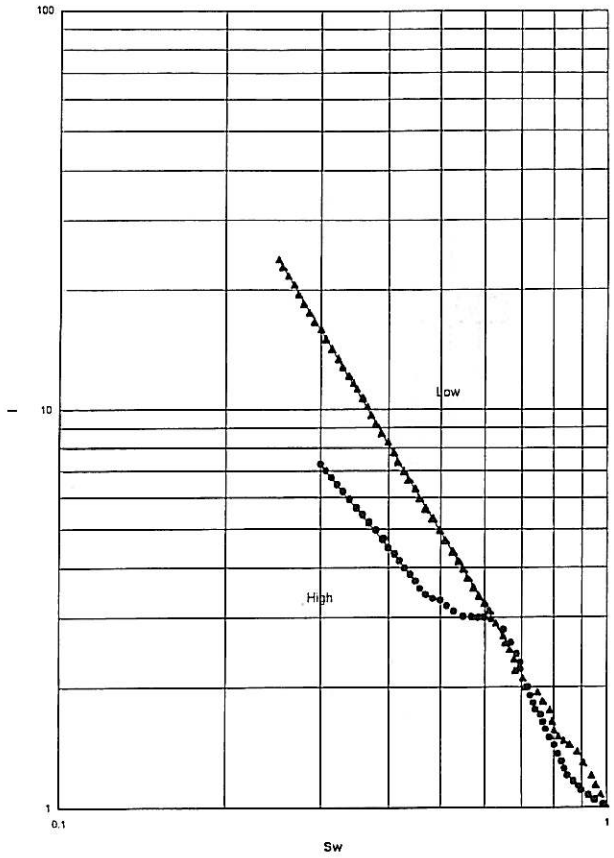


Fig. 4. I *vs* Sw for sample 2 at low and high viscosity ratio.

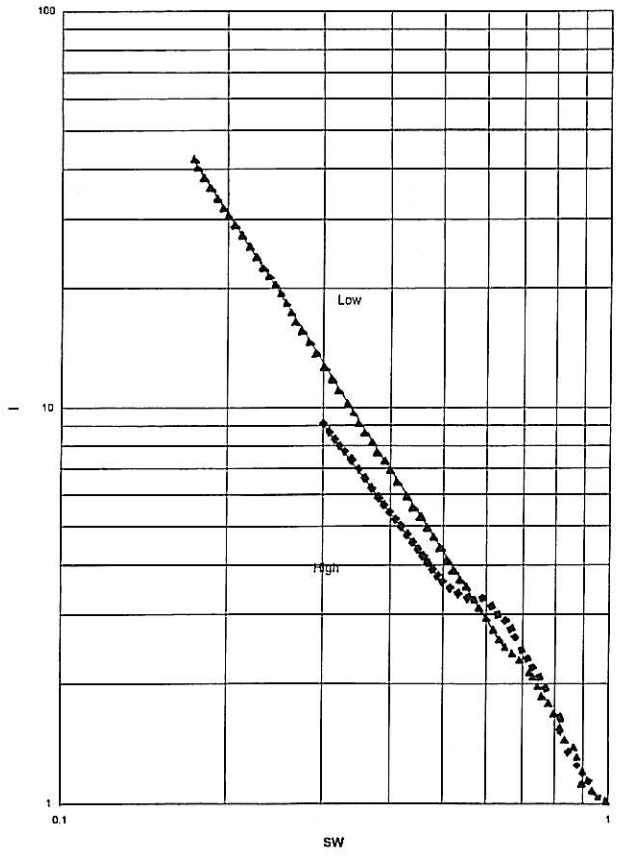


Fig. 3. I *vs* Sw for sample 1 at low and high viscosity ratio.

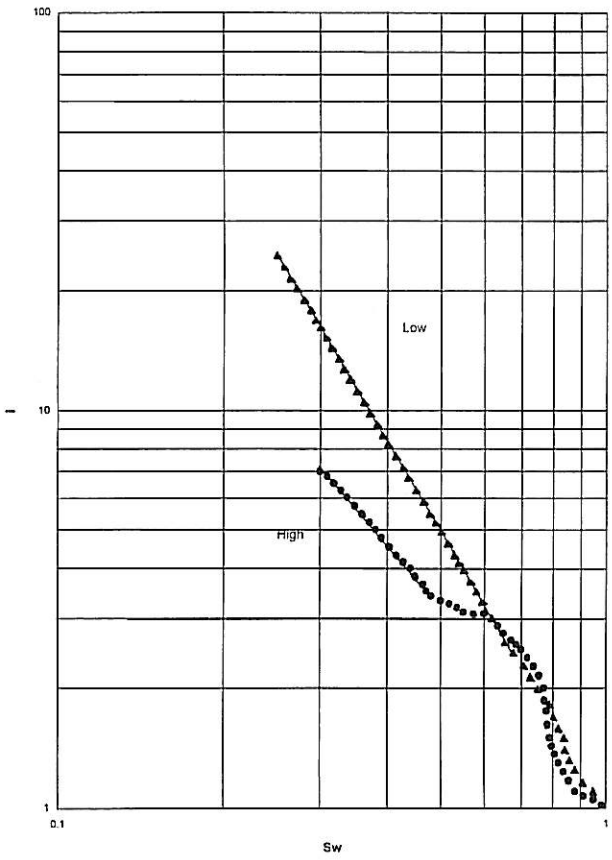


Fig. 5. I *vs* Sw for sample 3 at low and high viscosity ratio.

These high differences confirm the necessity to perform resistivity index measurements with fluid that have the same characteristics as the fluids of the reservoir or the formation under investigation.

CONCLUSIONS

The influence of viscosity ratio on the resistivity index versus brine saturation relation has important consequences for saturation exponent determination by the continuous injection technique. The results obtained above show that measurements of the resistivity index by the continuous injection technique using a fixed viscosity ratio may give an unrepresentative value of n, and lead to error in Sw determination. Such measurements should be carried out at a viscosity ratio represented by the active reservoir viscosity ratio in order to obtain a reliable value of n. As a result of this study, it has been found that the use of low viscosity ratio gives a different relationship of *I* versus Sw compared to the high viscosity ratio. It is also found that a linear relation of *I* versus Sw is obtained at low viscosity ratio and this is due to the existence of a more uniform saturation distribution throughout the core sample. The value of saturation exponent to be used in water saturation determination should be treated with extra care since fluid characteristics created in the laboratory may not be the same as in the reservoir.

ACKNOWLEDGEMENT

The authors wish to thank the Robert Gordon University for permission to publish this work. Special thanks goes to Core Laboratories, Aberdeen for their help in providing the laboratory facilities. The support of the Libyan Higher Education People Committee is gratefully acknowledged for sponsoring Mr. Al-Mahtot during his postgraduate program.

REFERENCES

[1] Archie G.E., 1942. The electrical resistivity log as an aid in determining some reservoir characteristics, *Trans, AIME*, **146**, 54.

[2] de Waal, J.A. Smits, R.M., de Graaf, J.D. and Schipper, B.A., 1991. Measurements and evaluation of resistivity index curves. *The Log Analysts*, (Sept.-Oct.), 583-595.

[3] Grattoni, C.A. and Dawe, R.A., 199 . Electrical resistivity and fluid distribution of coexisting immiscible phases. Paper No. 9625 SCA Conference, Montpellier, France, 9-13 Sept.

[4] Morrow, N.R., 1990. Wettability and its effect on oil recovery, *JPT*, (Dec.), 1476-1484.

[5] Zeelenberg, P.W. and Schipper, B.A., 1992. Developments in I-Sw measurements. *3rd European Core Analysis Symposium* (EUROCAS III), Paris, Sept. 14-16.

[6] Arps, J.J., 1953. The effect of temperature on the density and electrical resistivity of sodium chloride solutions, *Trans. AIME*, **198**, 327-330.

[7] Hawes, R.I, Dawe, R.A., Evans, R.N. and Grattoni, C.A., 1995. The depressurization of water-flooded reservoirs-wettability and gas saturation, *J. of Petrol Geos.*, **2** (May), 117-124.

Petroleum Res. J. Vol. 10 (1998); P. 13-15, 1 Fig.

Effect of Porosity Type Upon Archie's Parameters of Carbonate Reservoir

O.B. Al-Mahtot*, W.E. Mason* and M. Nasar**

تأثير نوع المسامية على مُعامل التشبّع في معادلة Archie

عمران المحتوت و و.ي. ميسن و محمد نصر

تعتبر معادلةArchie المعادلة المستخدمة لحساب معامل التشبع المائي n, m تساوي 2.

تم إجراء تجارب معملية لحساب معامل التشبع ومعامل الإلتحام لمكامن جيرية مختلفة المسامية وذات مجال واسع بحوض سرت بليبيا. تم تجميع عدد عشرة عينات لبيّة من عدة طبقات جيرية ذات مسامية متباينة ومن مواقع متباعدة، كما تم قياس مقاومة التيار الكهربائي بواسطة اللوح المسامي. أثبت نتائج التجارب أن قيمة n تتغير ويمكن أن تكون أقل أو تساوي 2 بينما قيمة n يمكن أن تصل إلى 2.78 واستنتج أن قيم m و n تعتمد على مسامية الصخور. كما أن علاقة التشبع المائي مع مقاومة الصخور للتيار الكهربائي تتفق تماماً مع معادلة Archie بإستثناء الصخور المسامية التي وجد أن قيمة n تصل بها إلى 2.78.

توصى هذه الدراسة بإجراء قياسات لتحديد قيمة m و n لعدة عينات صخرية من كل طبقة تتغير فيها المسامية بدلاً من إستخدام قيم ثابتة لكامل التكوين الجيولوجي.

Abstract: *Water saturation determinations from resistivity logs are based on Archie's equation; $Sw = (\phi^{-m} Rw/Rt)^{1/n}$. The cementation factor m, and saturation exponent n play an important role in Sw calculation. In carbonate formations m = n = 2 is usually used. However, m values between 1.88 and 2.5 have been measured, and also n was found to be between 2.11 and 2.78 for a Libyan carbonate reservoir. Incorrect m and n would lead to large inaccuracies in the calculated hydrocarbon/water saturation.*

An experimental study was carried out to measure m and n for carbonate samples with a wide range of porosity and permeability. Ten samples were collected from a formation having vuggy and interparticle porosity types. The resistivity measurements were performed using the porous plate method, with four-electrodes system. Reservoir fluids are simulated using a brine and oil of the formation of interest. As a result of this study, it has been found that the Archie's parameters are functions of pore structures. Samples, mainly with interparticle or intercrystalline porosity, shows m-value to be less than or equal to 2, while vuggy samples generate high values of m. The resistivity/saturation correlation is well fitted by Archie's law except for vuggy samples, where n was found to be as high as 2.78. As a consequence, it is recommended that in order to evaluate cementation factors and saturation exponent for carbonates, representative numbers of samples from each zone or interval porosity type should be used rather than an average of m and n of the whole formation.

INTRODUCTION

Carbonate formation may have several types of porosity which includes interparticle, vuggy,

*Al Fateh University, Petroleum Department, Tripoli, Libya (GSPLAJ)
**The Robert Gordon University, Aberdeen, U.K.

moldic and fracture porosity as classified by Choquette and Pray[1] and discussed by Rieke *et al.*[12]. Many investigators studied the Archie parameters[3] of carbonate formation with focus on the influence of porosity type[4,5,6]. However, as a result of these studies, many other approaches were derived such as the empirical approach (Shell formula[7], Borai correlation[8]). Although these approaches were successful in many cases but do not take in account the fact that the Archie parameters (m and n) may vary in the same way as porosity and lithology[9]. A case study is presented in this article to contribute somehow to the carbonate formation evaluation.

EXPERIMENT

The formation resistivity factor and resistivity index were measured in the laboratory at ambient conditions for $1^1/_2$" diameter for ten carbonate samples. Their physical properties are shown in Table 1.

Table 1. Core plugs properties

Sample No.	ϕ(%)	K(mD) (gm/cc)	G.D
1	20.34	2.37	2.84
2	12.43	3.3	2.84
3	16.2	31	2.86
4	27.92	158	2.86
5	10.84	0.25	2.84
6	37.36	145	2.85
7	11.12	1.46	2.84
8	26.33	3.58	2.84
9	31.21	6.94	2.85
10	13.25	10.3	2.84

These plugs have been collected from a Libyan reservoir in the Sirt Basin. The samples were cleaned in hot solvents, dried and then mounted into the core holder. All samples were saturated with brine (80,000 ppm). The resistivity measurements were performed using the 4-wire method which has the advantage of eliminating end effects. The resistivity of the saturated samples (Ro) and brine resistivity (Rw) were measured on consecutive days until the results were stabilized. The resistivity index measurements were carried out using the porous plate method, in order to compare it with continuous injection technique results. In this method, the resistivity measurements and desaturation process takes place separately. The samples were desaturated simultaneously by placing them on a porous place in a pressure cell, and gas pressure was applied. The gas (nitrogen) enters the samples from all directions except from the end face. The gas pressure was maintained until no more brine was produced. After capillary equilibrium was reached, the gas was then released and the samples removed from the pressure cell and weight measurements were taken as well as resistivity readings. The procedure was repeated for several pressures in the range of 0.5 psi to 180 psi. The desaturated process for each sample typically took 4-5 days to complete. Finally, m was calculated (m = -logRo/Rw/log ϕ) as well as n being (n = - logRt/Ro/log Sw).

RESULTS AND DISCUSSION

Figure 1 shows the relation of log F versus log ϕ for all samples. Table 2 represents m and n values of all samples.

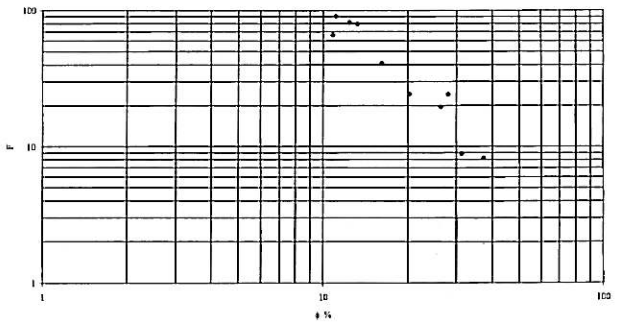


Fig. 1. Formation factor *vs.* porosity

Table 2. m and n values for all samples

Sample No.	m value	n value
1	2.01	2.31
2	2.11	2.46
3	2.05	2.11
4	2.5	2.78
5	1.86	2.14
6	2.14	2.48
7	2.06	2.26
8	2.23	2.34
9	1.88	2.51
10	2.17	2.46

Archie's equation obtained for this reservoir by averaging m an n values was $Sw = (\phi^{-2.1} Rw/Rt)^{1/2.39}$. This cementation factor values were close to each other and m ranged from 1.88 to 2.5. However, higher m values were found in vuggy samples such as samples 4 and 9 and m values were around 2 for interparticle type porosity (samples 1, 3 and 7). The saturation exponent values were between 2.11 and 2.78. It is observed that high n values were found associated with vuggy samples such as samples 4, 9 and 10. Lower n values were generated for interparticle porosity type samples (sample 3 and 5). These findings suggest that the assumption of m=n=2 for carbonates is inaccurate because m and n depend on a type of porosity which exists in a zone or formation. This assumption is valid for a reservoir with only interparticle or intercrystalline porosity type. The error in water saturation determination could reach even 20% and a decision to consider a zone or formation is dry or productive would be in great risk. Table 3 shows Sw values calculated and error in it; when m, and n assumed to be constant and when they are variable.

Table 3. Sw calculations at different m and n

Sample No.	m=n=2	m, n variable	ΔSw%
1	24.58	29.9	5
2	51.36	63.86	12.5
3	30.86	34.26	3.4
4	22.86	43.51	20.65
5	58.9	52.72	6.18
6	13.38	20.88	7.5
7	57.41	64.87	7.46
8	24.24	33.96	9.72
9	20.45	19.07	1.4
10	37.74	52	14

CONCLUSION

In carbonate reservoir evaluation, the Archie's parameters has a wide variation depending on the pore structure (porosity type). It is concluded that the vuggy samples generate higher m and n than the interparticle porosity type samples. It is recommended that samples representing each porosity type should be used rather than an average of m and n of the whole formation.

ACKNOWLEDGEMENT

The authors wish to thank Corex (UK) for their permission to use the laboratory facilities. Also, thanks goes to R.G. University for their permission to publish this article.

REFERENCES

[1] Choquette, P.W. and Pray, L.C., 1972. Geologic nomenclature and classification of porosity in sedimentary carbonates. *Bull. Am. Assoc. Petrol. Geol.*, **54**, No. 2, 207-250.

[2] Rieke, H.H., Chilinger, G.V. and Munnon, R.W., 1972. *Oil and Gas Production from Carbonate Rocks*. Elsevier Publishing Company, Inc. New York.

[3] Archie, G.E., 1942. The electrical resistivity log as an aid in determining some of the reservoir characteristics, *Trans AIME*, **146**, 54.

[4] Focke, J.W. and Munn, D., 1987. Cementation exponent in Middle East carbonate reservoirs. *SPE Formation Evaluation*, (June).

[5] Nurmi, R.D., 1984. Carbonate pore system: porosity-permeability relationship and geological analysis. *Am. Assoc. Petrol. Geol.* Annual Meeting, San Antonio, (May).

[6] Aguilera, R., 1980, *Naturally Fractured Reservoirs*, PennWell Publishing Company.

[7] Neustaedter, R.H., 1980. Log evaluation of deep Ellenburger gas zones, SPE paper 2071 presented at the Deep Drilling and Development Symposium-Delaware Basin of the SPEC of AIME, Monahans, Texas, (March).

[8] Borai, A.M., 1987. A new correlation for the cementation factor in low-porosity carbonate, *SPE* Formation Evaluation, (Dec.), 120-132

[9] Watfa, M. and Nurmi, R., 1987, Calculation of saturation, secondary porosity and productivity in complex Middle East carbonate reservoirs. Paper presented at the 28th SPWLA Annual Logging Symposium, (June-July).

Petroleum Res. J. Vol. 10 (1998); P. 17-24, 13 Figs.

Simulation of New Technique for Measuring Relative Permeability and Capillary Pressure at Capillary Dominated Flow

Mabruk A. Benrewin*

طريقة جديدة لِمحاكاة قياس النفاذية النسبية والضغط الشُعيري

المبروك أحمد بن روين

تعتمد طريقة تمييز نوعية التبلّل للصخور المسامية على قياس النفاذية النسبية للصخور والضغط الشعيري في وقت واحد وتحت تأثير السريان الشعيري.

أكدت نتائج المحاكاة وتحت ظروف تبلل مختلفة إمكانية تطبيق هذه الطريقة الجديدة لتعيين نوع التبلل للصخور معملياً تحت ظروف خاصة.

Abstract: *A novel technique of characterizing wettability of porous media is based on simultaneous measurement of relative permeability and capillary pressure under capillary dominated flow. A simulation study was conducted under different wettability conditions and model results confirmed that the proposed scheme can be implemented in the laboratory.*

INTRODUCTION

The development of this new technique was based on recent network modeling study by McDougall and Sorbie[1,2]. They found that representing the relative permeability functions in the conventional way as a function of wetting phase saturation essentially "hides" the processes that are going on at the pore scale. The network predictions have suggested that, plotting oil relative permeability, Kro, as a function of the reciprocal of capillary pressure, $1/P_c$, enables the interpretation of the effects of pore scale physics. As a result of these findings, an experiment has been designed to measure relative permeability and capillary pressure simultaneously so that the proper plots can be generated. A schematic diagram of the apparatus is shown in Figure 1. The basic idea, in this new technique, is to carry out carefully controlled measurements under conditions of capillary equilibrium; this involves making such measurement with pressure regulation in each of the oil and water phases using the Back Pressure Regulators (BPR) system. The essential sequence of measurement is:

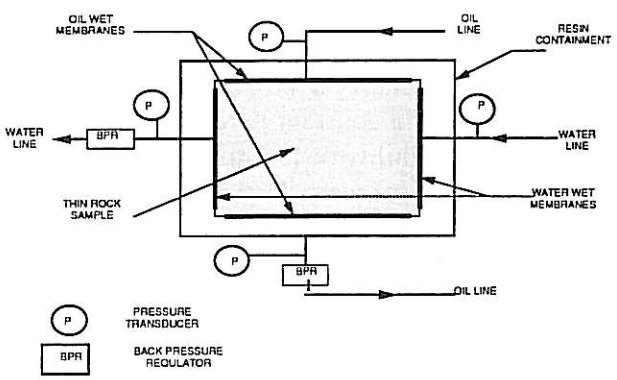


Fig. 1. Schematic diagram of the experiment

*Petroleum Engineering Dept., Al Fateh University, Tripoli, Libya

(i) – Set the oil and water pressures on the separate BPRs, thus setting the capillary pressure, Pc.

(ii) – Flow the oil and water separately until the equilibrium are reached *i.e.* a steady-state fluid distribution in the small sample.

(iii) – Carry out the measurements of relative permeability at a given capillary pressure by setting the flows at appropriate levels, controlling the BPRs and measuring the pressure drops and flow rates.

A small size sample ensures that capillary equilibrium can be established quite rapidly so that many measurements can be made in a short period of time. In the work reported here, the main objective is to evaluate the proposed experimental approach numerically. This allows us to examine various procedures for the proposed experiments before trying to carry them out in the laboratory. In this study the modeling of the new technique was carried out using the Eclipse-100 black oil simulator.

MODEL DESCRIPTION

A numerical model was constructed using the Eclipse simulator to simulate the new experiment as proposed by McDougall and Sorbie[1,2]. The model layout is shown in Figure 2. It is a two-dimensional model (X-Y) composed of 100 grids, four of them non-active. The numbers of grids in both directions are set equal to 10 and have equal dimensions in both directions. The porous medium is represented by a two-dimensional square horizontal section and has dimensions of 0.8 cm by 0.8 cm and a thickness of 0.1 cm. this small section is necessary to achieve capillary equilibrium in a short period. The porous medium was assigned to a constant porosity of 20%, and absolute permeability of 100 mD. The wetting an non wetting phases were dead oil and water with identical density and viscosity of 1gm/cc and 1 cp. respectively. Each phase flow in one direction; independently of one another, *i.e.* they are not injected simultaneously from one side of the sample as it used to be in the other methods of measuring relative permeability. This will allow the potential drop of each phase measure independently.

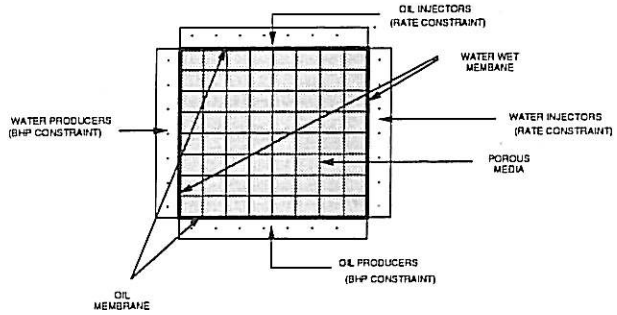


Fig. 2. Model layout

The injecting oil lines and water lines are represented by tiny horizontal wells that are in direct contact with the porous media through the semi-permeable membranes. The injection wells are controlled by rates and at each capillary equilibrium they are subjected to variable rates. Producing oil and water lines are also represented by horizontal wells and they are controlled by bottom hole pressures to represent the back pressure regulators. It is assumed here that by setting a back pressure on each line, the differences in the pressure between the oil lines and water lines will set the capillary pressure in the porous system.

Semi-permeable membranes are essential elements of the experimental set-up and were simulated using the concept of directional relative permeability. The main components of the input data are the capillary pressure and the relative permeability data which control the fluids distribution and their relative flow in the system. Table 1 gives the equations used to generate input data under different wettability conditions.

Table 1. Input capillary pressure and relative permeability data

Water-wet System:

$Krw = 0.30\ Se^3$
$Kro = 0.85\ (1\text{-}Se)^3$
$Pc = 3.0\ (\quad)^{0.5}\ (Se)$

Where

$Swc = 0.6 - 0.165 \log (Kabs)$
$Swor = 0.7$

Oil-wet System:

$$Krw=0.8\ Se^2$$
$$Kro=0.85\ (1-Se)^3$$
$$Pc=0.26038-5.652Sw+42.50Sw^2-148.44Sw^3+243.355Se^4-152.89Sw^5$$

Where

$$Swc=0.30$$
$$Swor=0.65$$

Mixed-wet System:

$$Krw=0.45\ Se^2$$
$$Kro=0.70\ (1-Se)^{2.75}$$

- Capillary pressure for the imbibition curve:
  $Pc=15.78-112.47Sw+268.0Sw^2-213.33Sw^3$
- Capillary pressure for drainage curve:
  $Pc=0.220085-2.7945Sw+9.7049Sw^2-10.263Sw^3$

Where

$$Swc=0.30$$
$$Swor=0.70$$

$$Se=\frac{Sw-Swc}{Swor-Swc}$$

SIMULATION STRATEGY

At any stage of the simulation process, the outlet boundary conditions (represented by the bottom hole pressure of the oil and water producers) were set to impose a back pressure equivalent to a certain capillary pressure. Thus, for a fixed capillary pressure, (P_o-P_w), as steady-state saturation in the system can be reached.

Equilibrium conditions can be achieved by flowing both phases at low rates. When the pressure gradient of each phase is kept virtually unchanged across the system and the saturation distribution becomes uniform (for a homogeneous system), this indicates that equilibrium has been established in the system at that specific capillary pressure. The relative permeability of each phase can be measured independently at the equilibrium conditions by keeping the outlet boundary conditions fixed and gradually raising the flow rate of one of the phases until the pressure drop across the sample can be measured. After that, the flow rate is again gradually reduced until it returns to the initial (equilibrium) condition. This process can be repeated for the other phase. During this process, it is assumed that the saturation is uniform (for a homogeneous system) and maintained at equilibrium conditions fixing the capillary pressure.

If the water phase is to be allowed to imbibe into the system, the capillary pressure between the water phase and the oil phase should be reduced which can be done whether by decreasing the oil potential or by increasing the water potential.

RESULTS

The results from the simulation runs have shown that capillary equilibrium can be established which is characterized by uniform fluid saturation distribution in the system. Figure 3 shows the water phase saturation distribution at different capillary equilibrium for the water-wet system. Water saturation distribution at each equilibrium was within 1% differences over the whole system which is an acceptable tolerance for these types of experiments. The difference in

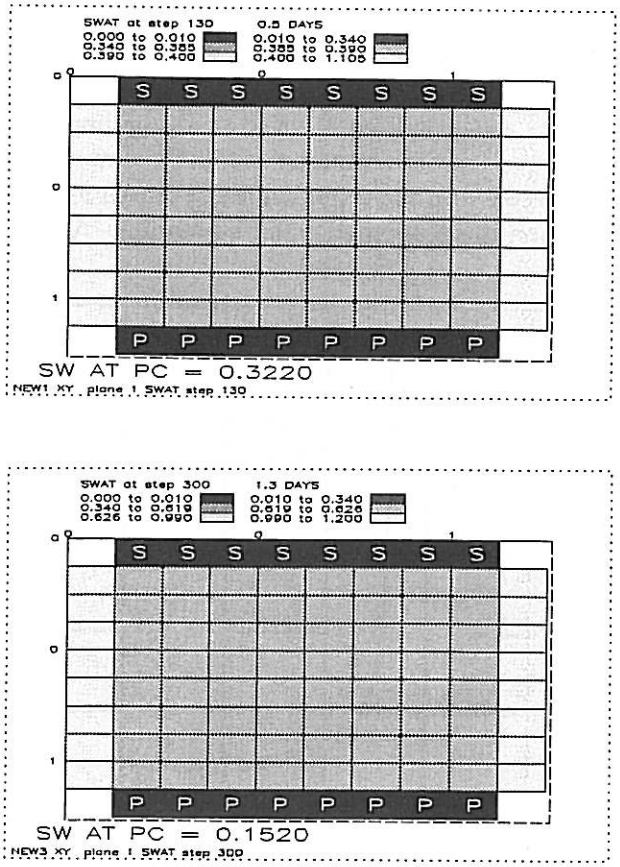


Fig. 3. Water-wet system

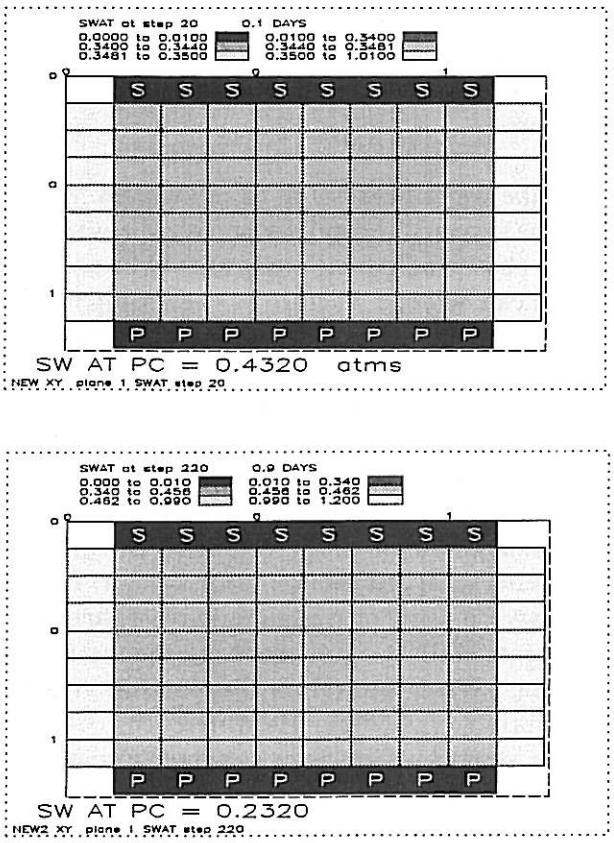


Fig. 3. Water-wet system

the pressure between the phases at the outlets was assumed to represent the capillary pressure in the system and it will be referred to as the imposed back pressure. The imposed capillary pressure was compared with the input capillary pressures as a function of he average water saturation. A very good match has been obtained for each wetting condition as shown in Figures 4,5,6.

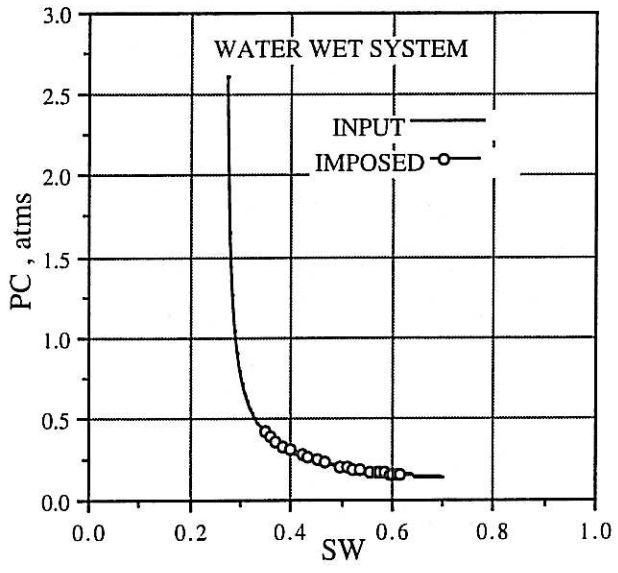


Fig. 4. Input *vs.* imposed capillary pressure

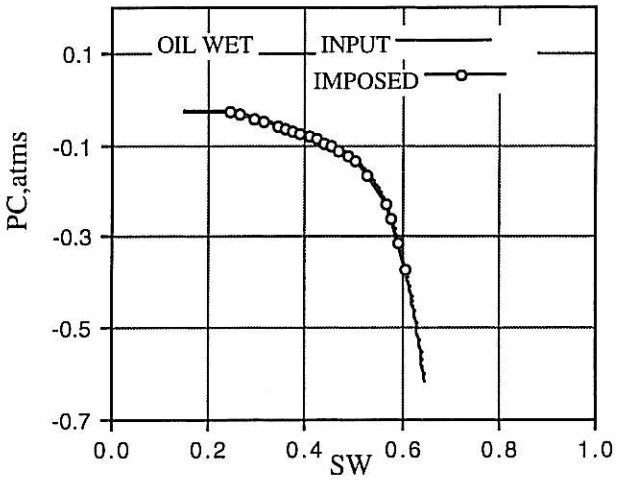


Fig. 5. Input *vs.* imposed capillary pressure

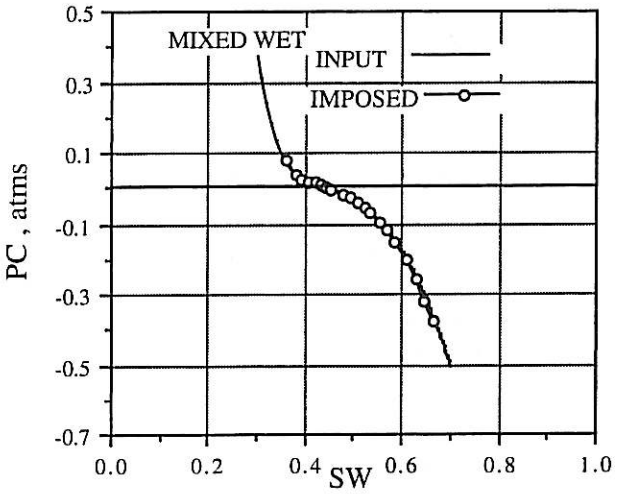


Fig. 6. Input *vs.* imposed capillary pressure

The model was also run to investigate the effect of the rising flow rate of one of the phases on the equilibrium condition. Figure 7 shows the effect of increasing oil rate on the saturation distribution for the water-wet system. First, the system is at an equilibrium then the rate is raised five times, at this stage the saturation distribution has been changed but within very small variations then the rate was increased 10 times and also a change in the saturation distribution has been observed but still within an acceptable range. Finally, the rate is reduced to its initial conditions (base case) where a complete re-establishment is obtained.

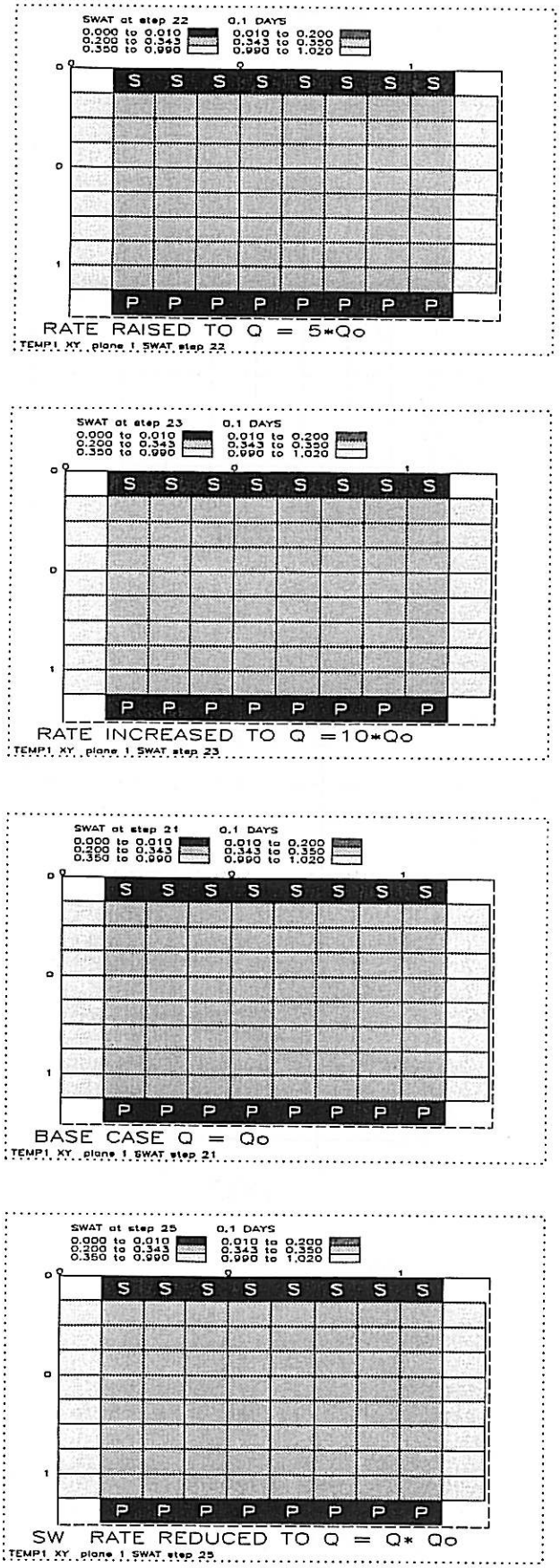


Fig. 7. Oil rate increased at constant PC

Darcy's law was used to calculate the relative permeability for each phase. These calculated relative permeabilities were compared with the input relative permeabilities (Figs. 8, 9, 10). All figures show a very good agreement that is achieved between the input and computed relative permeability data.

One of the advantages of using the simultaneous measurement of capillary pressure

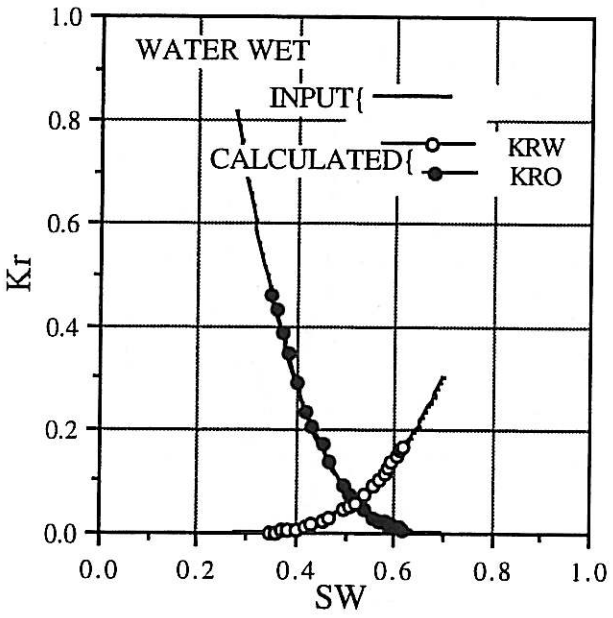


Fig. 8. Input *vs.* calculated relative permeabilities

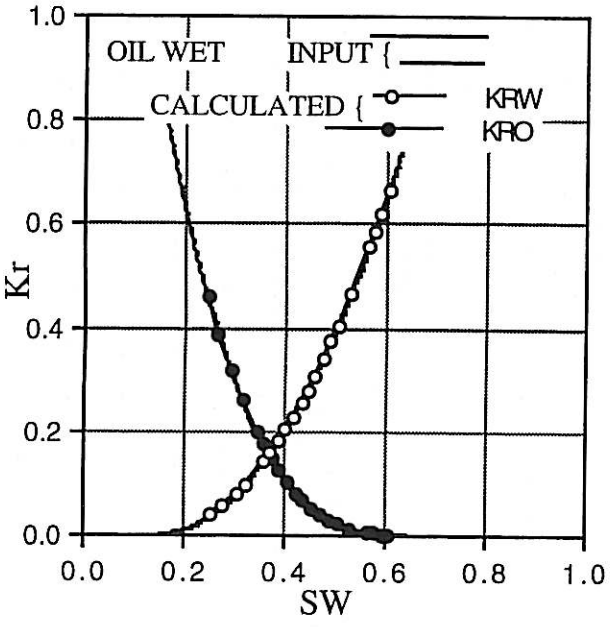


Fig. 9. Input *vs.* calculated relative permeabilities

and relative permeability is to use this data to plot the oil relative permeability as a function of he reciprocal of the capillary pressure to indicate the type of wettability in the system. Figures 11, 12, 13 show the plot between the inverse of the imposed capillary pressure with respect to the calculated relative permeabilities under different wettability conditions.

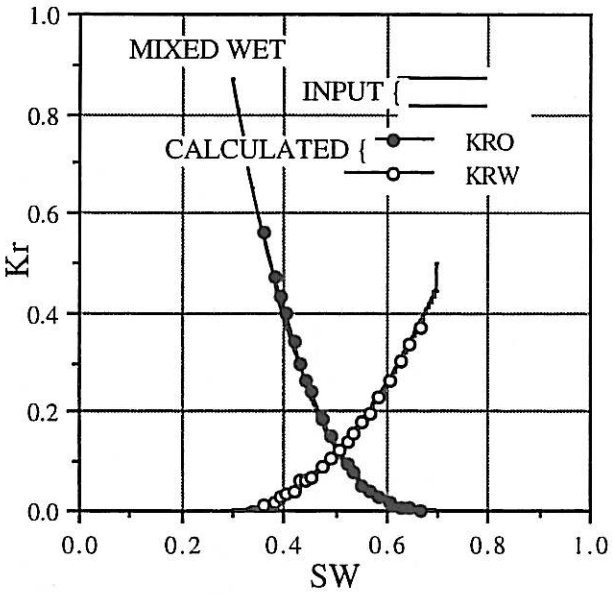


Fig. 10. Input *vs.* calculated relative permeabilities

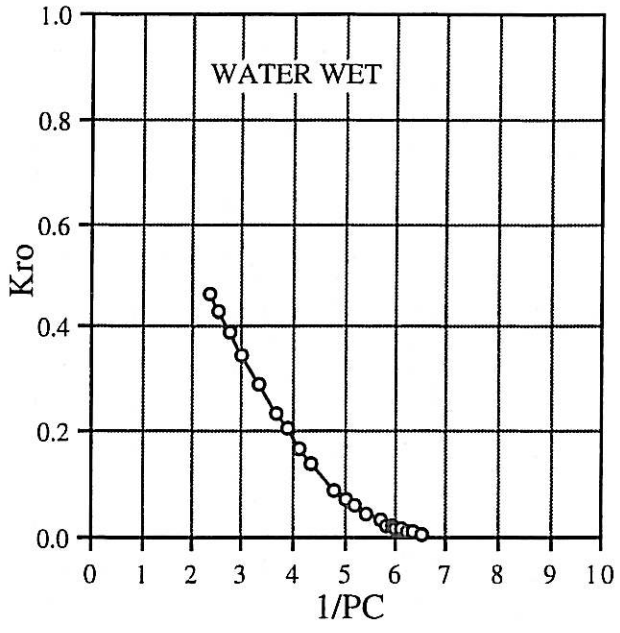


Fig. 11. 1/PC *vs.* Kro

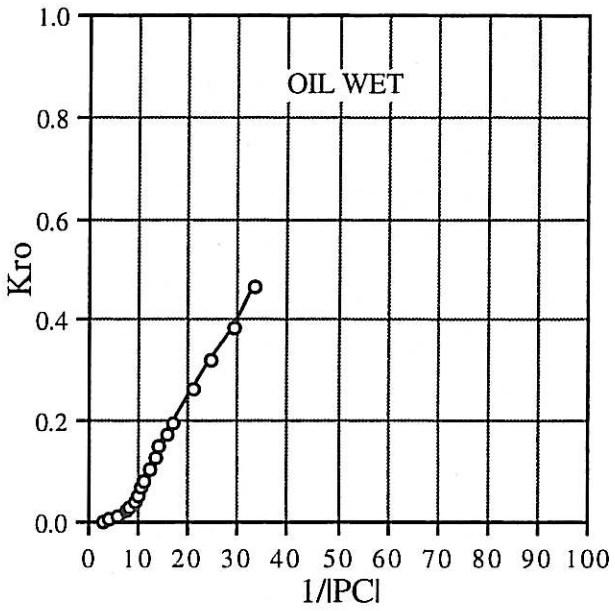


Fig. 12. 1/|PCI *vs.* Kro

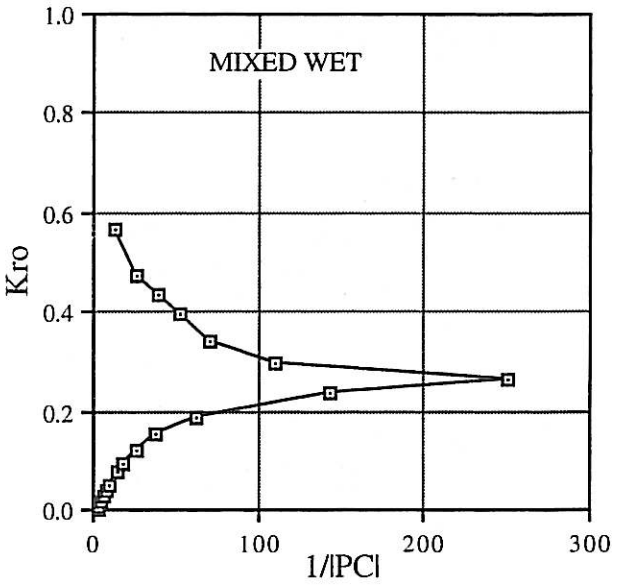


Fig. 13. 1/|PCI *vs.* Kro

DISCUSSIONS

In general, the model has been able to show clearly that capillary equilibrium can be established at dynamic conditions i.e. both phases can flow simultaneously while the saturations are held constant. Figure 3 shows the saturation distribution at different capillary pressure for the water-wet system. These rather featureless figures can be understood as follows: at Pc=0.432

(Atmospheres=6.65 psi) where the grey shading is for the saturation range 0.344 and 0.348; clearly, all the region is within this "contour" or shading. This is, in fact, the appropriate saturation at capillary equilibrium from the (input) capillary pressure curve. The other figures have been plotted in this way i.e. the shaded range closely brackets the expected saturation at capillary equilibrium.

The difference in the outlet boundary pressures impose a back pressure on the porous media equivalent to the capillary pressure between the phases. Figures 4, 5, 6 show an excellent agreement between the input capillary data. These indicate that, by measuring the difference in the pressure at the outlet, boundaries may enable us to measure the capillary pressure and to establish a constant equilibrium saturatio in the system. This concept may be well suited in small and thin samples, where the saturation gradients are small.

The model was also run to investigate the effect of rising the flow rate of one of the phases on the equilibrium condition. Figure 7 shows the results obtained for the water-wet system. First, the model was run at low rates for both phases and at fixed capillary pressure until equilibrium was established (the base case). The rate of one of the phase was then raised until the steady-rate conditions were achieved. After that, the rate is reduced to the base case where the same process is repeated for the other phase. It is this process of raising the flow rates that allows us to measure the corresponding relative permeabilities at the established capillary equilibrium. As soon as the rate of any phase is raised, while the back pressure is kept constant, a saturation gradient in the direction of the flow of that phase may be developed in the system. These saturation gradients were a result of an increase in the viscous force. If that force was controlled and carefully monitored just to make the pressure drop measurable, the differences in overall average of saturation in the porous media will be minimum and the system may be considered as if it is still in its equilibrium conditions. In order to sustain equilibrium conditions, the rates should be raised gradually until the pressure gradient across the sample for any phase reaches the level that can be measured (it must be greater than 0.01 psi). This procedure will avoid unnecessary rate increases that may cause high saturation gradient in the system.

Most of the results obtained under different wetting conditions show a slight difference in saturation distribution (less than 2% pore volume) which can be accepted as technical errors in the "experiment". In most of the steady-state methods, the average saturation agreed within 2% pore volume (McCaffery and Bennion[3], Honarpour *et al.*[4]).

The other interesting point from these processes is that the initial equilibrium conditions (base case) can be re-established after the rate is raised and the process can be repeated for the other phase. This condition enables the measurement of the relative permeability for both phases at fixed capillary condition and this is one of the most important tasks in this experiment.

According to the proposed experiment, the relative permeabilities should be measured simultaneously with the capillary pressure. The model has performed the above requirements by first establishing capillary equilibrium and then calculating the relative permeability of each phase using Darcy's law under steady-state condition. All the results were compared with the input relative permeability data as shown in Figures 8, 9, 10. Although the overall agreement is good, the simulation results show better agreement away from the end points. Near the end points, the viscous pressure gradients were high as a result of low relative permeability of one of the phases which cause high saturation gradient in the system.

One of the advantages of the new experiment is to detect the type of wettability from the plot of the reciprocal of the capillary pressure versus the oil relative permeability. The results obtained from the model outputs were used to check whether the trends that have been presented by McDougall and Sorbie[2] can be reproduced using this large scale model. Calculated oil relative permeabilities were plotted against the reciprocal of the capillary pressure as shown in Figures 11, 12, 13. The trend of the water-wet curve was identical to that predicted by network modeling for an imbibition process. For the oil-wet, the drainage process of the oil-wet system has not been presented by the network modeling and there

is no comparison to be made, but it is believed that this trend is completely different from the water-wet system and can be used as a good indication of the type of wettability. The shape of the curve for the mixed-wet system is characterized by two trends. One represents the imbibition processes which lie in the positive section of the capillary pressure curve and the other represents the forced imbibition curve which lies in the negative side of the capillary pressure curve. The imbibition part of the mixed-wet system was identical to the ones predicted by the network model. The forced imbibition curve is identical to the trend of the drainage curve of the oil-wet system. Since the data used is not representative of actual cases, it is recommended to investigate the above trends with measured data under different wetting conditions.

The results have confirmed the possibility of carrying out the proposed experiment in the laboratory although a number of practical conditions may have to be investigated. In particular, the minimum rates that can be achieved practically. Model results have indicated that low rates are essential to establish capillary equilibrium. Those rates were ranging from high values as 0.1 cc/hr to low values as $1X10^{-4}$ cc/hr and depends mainly on the input petrophysical properties of the porous system. Low rates such as $4X10^{-3}$ cc/hr can be attainable in the laboratories (Kokkede and Boutkan[5]). It was found that increasing the number of wells representing the flow lines improves the intake rates into the system without distributing the capillary equilibrium. The model may be used as a good tool to determine the appropriate rate for the experiment if other relevant data are available. The mechanism on which the experiment has to be run was well simulated and procedures can be set for the experiment if the model is supplied with actual data. The semi-permeable membranes are an essential part of the experimental set-up and should be carefully selected to satisfy the boundary conditions.

CONCLUSIONS

A model was set up according to the proposed experimental scheme. The following conclusions were drawn from the simulation study:

1 - The results have confirmed the possibility of carrying out the proposed experiment in the laboratory although a number of practical conditions may have to be investigated.
2 - Relative permeability for oil and water phases can be measured at a fixed capillary pressure using the proposed scheme: i.e. by achieving capillary equilibrium and then raising the flow rates of the two phases separately. This technique will enable the representation of oil relative permeability as a function of reciprocal of capillary pressure that gives a good indication of what is going on at the pore-scale level.
3 - More studies are required at different wettability conditions in order to set-up a general trend for wettability characterization using actual data.
4 - Modeling the proposed experiment numerically is useful in that it may assist in establishing procedures for the experiment. Also, if such experiments are actually conducted, the model can be used to match the results.
5 - If such experiments prove to be practical, then a new technique may emerge for measuring relative permeabilities and capillary pressure simultaneously to detect the type of wettability in porous media.

REFERENCES

[1] McDougall, R.S. and Sorbie, K.S., 1992. *Network Simulation of Flow Processes in Strongly Wetting and Mixed-wet Porous Media.* 3rd European Conference on Mathematics of Oil Recovery, 17-19 June, 1992, University of Delft, Netherlands, 169-181.

[2] McDougall, R.S. and Sorbie, K.S., 1993. The prediction of waterflood performance in mixed-wet systems from pore-scale modeling and simulation. SPE 25271, paper presented at 12th SPE Symposium on Reservoir Simulation, New Orleans, Feb 28-Mar.3, 1993.

[3] McCaffery, F.G. and Bennion, D.W., 1993. The effect of wettability on two-phase relative permeabilities. *J. Cdn. Pet. Tech.*, (Oct-Nov, 1974) **13**, 42-53.

[4] Honarpour, M., Koederitz, L.F and Harvey, A.H., 1986. *Relative Permeability of Petroleum Reservoirs*, CRC Press Inc., Boca Raton, Fl.

[5] Kokkede, J.K. and Boutkan, V.K., 1995. Toward measurement of capillary pressure and relative permeability at respective wettability. In H.J. (ed.) *New Development in Improved Oil Recovery*, Geo. Soc. Spec. Publ., No. **84**.

Petroleum Res. J. Vol. 10 (1998); P. 25-29, 2 Figs.

Evaluation of Clay and Drilling Fluid Quality

Talal M. Mohammed* and A.G. Alrabti**

تقييم نوعية سائل وطينة الحفر

طلال مجيد محمد وعائشة جمعة الرابطي

تتناول هذه الدراسة تصميم نوموغرام يمكن إستخدامه في تقييم نوعية طينة الحفر الذي يعتمد بدورة على عامل الغرويّة ونسبة المواد الطينية النشطة كيميائياً ولزوجة سائل الحفر. كما يمكن إستخدام هذا النوموغرام في تقييم سوائل الحفر من حيث كمية المواد الصلبة المستعملة في تحضيره وتتبع عملية زيادة كثافة سائل الحفر للتأكد من أن كمية المواد الصلبة هي الكمية المثلى.
إستخدمت لغة البرمجة "C++" في تصميم النموغرام والحصول على النتائج الضرورية على هيئة رسوم توضيحية.

Abstract: *The present work is concerned with the construction of a nomogram, which can be used to evaluate the quality of clay materials. evaluation is carried out according to three parameters: Colloidity coefficient, fractional volume of active solid and mud viscosity. The constructed nomogram is also used to: Evaluate the quality of drilling fluid with respect to solid content, follow the process of increasing mud density to be sure the solid content is optimum. Design and drawing the proposed nomogram is carried out by using programming language "C ++".*

INTRODUCTION

It is well known that hydrophility of clay is the main physicochemical property that determines its suitability for drilling fluids preparation purposes. Basically, the hydrophility of clay depends upon: structure of clay minerals, specific surface area i.e. dispersion degree and Cation exchange capacity (CEC). The higher degree of dispersion, the higher CEC and the higher hydrophility, which leads to higher activity of clay particles. In order to evaluate the quality of clay and clay minerals, we should have quantitative parameter, which reflect their dispersion degree and chemical activity.

At the present time, the quality of clay is evaluated according to:

- Filtration and rheological properties of drilling fluids.
- Yield of clay.

In order to evaluate the dispersion degree of clay material quantitatively, the best method is adsorption of methylene blue (Mb). The methylene blue test measures the total exchange capacity of the clay system. CEC depends on the type and content of clay minerals present. The CEC is defined as cation-for-cation exchange between the clay building unit and a water solution, which contains the cation of greater attraction. CEC, which is reported in terms of milliequivalents (one meq = 120 ml.) of methylene blue per 100 grams of clay, is the relative ability of clays to carry exchangeable cations.

*Previously with Petroleum Engineering Department, Al-Fateh University, Tripoli, Libya
**Zuatina Oil Company, Tripoli, Libya.

The CEC is calculated, theoretically, as follows:

$$E = 10^5 \times \frac{S}{N \times \omega};$$

E - CEC of clay meq/100g;
S - specific surface area of clay m^2/g;
N - Avogadro's number = 6.02×10^{23}
ω - Surface area occupied by one cation of Mb = 95×10^{-20} , m^2

$$E = 0.175 * S$$

Inasmuch as specific surface area of pure montmorillonite is 800 m^2/g therefore;

$$E = 140 \text{ meq}/100g.$$

The following table shows typical CEC of different clays and drilled solids.

Table 1. CEC of various solids

Solids	Meq of Mb / 100g of solid
Montmorillonite	70 - 140*
Illite	10 - 40
Chlorite	10 - 40
Attapulgite (Sepiolite)	10 - 35
Koilinite	3 - 15
Gumbo shale	20 - 40
Sandstone	0 - 5
Shale	0 - 20

* Theoretically.

It is known from colloidal and drilling fluid chemistry that one gram of pure montmorillonite adsorbs ($59cm^3$) of methylene blue. This value ($59cm^3$), the author will consider as the standard to evaluate the relative activity of clay and drilled solids. Therefore, the quantitative parameter of clay quality will be represented by the colloidity coefficient "K". It describes the relative activity of clay and clay materials. "K" is defined as ratio of Mb adsorbed by one gram of a solid to ($59cm^3$) the amount of Mb adsorbed by one gram of pure montmorillonite;

$$K = V/59$$

K- Colloidity coefficient of tested clay.
V- Volume of Mb adsorbed by one gram of clay under consideration.

LABORATORY PROCEDURE OF Mb VOLUME DETERMINATION

In order to determine (V) the following procedure is used:

1. Prepare mud sample using clay of interest.
2. Add 1 ml of mud sample to 15 ml 3% of hydrogen peroxide and 0.5 ml of sulfuric acid. Boil gently for 3-4 minutes. After cooling dilute the mixture to 35 ml with distilled water.
3. Add Mb solution to flask. After each addition of 0.5 ml of dye, swirl the content of the flask for about 30 second and, while the solids are still suspended, remove one drop of fluid with the stirring rod and place the drop on the filter paper. The end point of the titration is reached when the dye spreads as a greenish-blue ring or tint around the spot of the dyed solids.
4. When the blue ring or tint is detected around the spot, shake the flask for additional 2 minutes and place another drop on the filter paper. If the blue ring is again evident, the endpoint has been reached, whereas if the ring does not appear, continue the addition of 0.5 ml Mb until a drop taken after shaking for 2 minutes shows the blue tint.
5. Report the "V" as volume of Mb which has been required to reach endpoint of titration.

Table 2 shows typical "K" values for different clay materials used to prepare drilling fluids in USA and (former) USSR.

Table 2. Typical "K" values

Clay material	Adsorption Mb			K = V/59
	cu. cm/g	g/g	Meq/100g	
Montehill	50	0.225	69.6	0.84
Heko	51	0.229	61.3	0.86
Bentonite	45	0.202	54.1	0.76
Cherkaski	44	0.198	52.8	0.74
Saragooski	46	0.207	55.3	0.78

Optimum Limit for "K"

The optimum limit of "K" is the practical limit, which is in turn, depended on particular downhole conditions, lithology, technical requirements and others. However the optimum range must be established. Therefore, and according to the value of "K" presented in Table 2 for most clay materials used in the mud preparation, clay with colloidity coefficient ranged between (0.7 - 0.75) is considered as good clay. Drilling fluid prepared with clay having "K" of (0.7) and greater is good with respect to:

- Rheological and filtration properties,
- Mud stability,
- Density regulation.

Calculation of Active Portion of Clay:

The fractional volume of active solids can be estimated as;

$$V1 = V / 59$$

V1- Fractional volume of active solid.

V- Volume of Mb required to reach endpoint.

The (V1) is expressed as a ratio of volume of active portion of clay to the total volume of clay i.e.

$$V1 = Vactive / Vclay$$

$$Vactive / Vclay = V / 59$$

V / 59 = K -Colloidity coefficient (by definition)

$$Vactive = K * Vclay$$

NOMOGRAM FOR QUICK EVALUATION OF CLAY AND DRILLING FLUID QUALITY

Preface:

The essential parameters for construction of nomogram are densities of clay, barite and water. Use of nomogram requires the laboratory predetermination of mud viscosity, mud density and total volume of solid. This nomogram is intended for determination of:

- Solid density,
- Volume of clay,
- Volume of barite,
- Colloidity coefficient,
- Volume of active portion of clay,
- Yield of clay. In addition, the nomogram can be used to aid the selection of optimum amount of bentonite and barite, which are added to increase the mud density.

Nomogram Construction:

The nomogram (Fig. 1)consists of three charts A, B, and C.

Data required for nomogram construction are Water, Clay and Barite densities. These charts were constructed as follows:

1 - Chart (A)

Illustrates the relationship between the mud density (Dm) solid volume (Vs) and solid density (Ds).

Each line in chart (A) represents constant solid density as a function of fractional solid volume and mud density. Solid density (For case of Vs = 30%, Vm = 1 cc and Dm = 1.5 g/cc) is obtained from the following expression:

$$Ds = (Dm * Vm - Dw * Vw) / Vs,$$

$$Ds = (1.5 * 1 + 1.03 * (1 - 0.3)) / 0.3 = 2.60 \text{ g/cc}$$

If the fractional volume of solid is decreased gradually from (0.30) until zero and (Ds) held constant the first (lower) line will be obtained. This line represents constant (Ds = 2.6 g /cc) as a function of different (Vs) and (Dm).

2 - Chart (B)

Chart (B) illustrates the relation between (Ds) and (Vc). In order to construct this chart, use a suitable scale to plot (Vc) on (x) axis as a function of (Ds). As solid density increased the (Vc) is decreased toward the upper left current, where the amount of clay is zero, whereas, the fractional volume of barite is 100%.

3 - Chart (C)

The relationship between mud viscosity, yield of clay and colloidity coefficient are shown in this chart. These relationships are obtained on the basis of laboratory experiments as a function of mud solid contents.

Examples

Ex. 1. ***Determination of clay and barite volumes***, colloidity coefficient , volume of active portion of solid, and yield of clay, assuming the following initial mud parameters:

- Mud density = 1.6 g/cc,
- Mud viscosity = 40 cp, and
- Total volume of solid = 20%.
- Volume of water is = 0.8 cc of water / 1 cc of mud. or 80%.

From point of intersection (of horizontal line of 1.6 g/cc and vertical line of Vs = 20%) draw line parallel to the nearest inclined line until intersecting with right (Y) axis of chart A. Read solid density (3.88 g/cc). From this point, draw a horizontal line into chart C until intersecting with inclined line of Vs%. From point of intersection, draw downward vertical until it intersects with the horizontal line representing mud viscosity of 40 cp. Read on the lower X axis of chart B clay volume (4.9% or 0.049 cc / 1 cc of mud). On the upper X axis of chart C read the yield of clay (60 bbl of mud of 40 cp per one ton of dry clay). Colloidity coefficient is 0.955. Thus, the amount of active solid is 0.049 * 0.955 = 0.0467 cc or 4.67%.

Barite volume is; 0.2 - 0.049 = 0.151 cc of barite / 1 cc of mud.

Weight of clay is 0.049 * 2.6 = 0.1247 gm.

Weight of barite is 0.151 * 4.3 = 0.6493 gm.

Total weight of solid is 0.1274 + 0.6493 = 0.7767 gm.

Density of solid is 0.7767 / 0.2 = 3.883 g /cc., which is very close to density obtained from nomogram (3.88 g / cc), error is 1%.

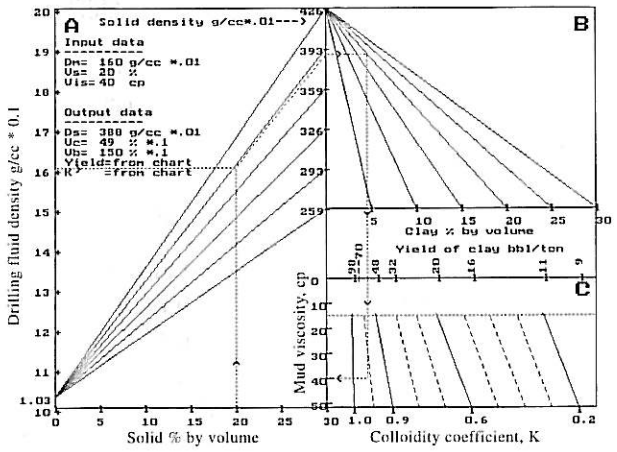


Fig. 1. Nomogram for evaluation of clay and drilling fluid quality.

Ex. 2. ***Follow the process of increasing mud density*** to be sure the solid content is optimal.

Situation:- The drilling below the intermediate casing requires an increase in the drilling fluid density from 1.6 to 1.8 g/cc. Show the optimum amount of solids required to increase the drilling fluid density.

Increase mud density usually is achieved by adding barite, but too much weighting material can cause the loss of the suspension system stability due to barite sedimentation. The final decision is dependent on field experience. However it is decided to use only barite for increasing the mud density. Let us refer to Figure 2. From this figure the following is obtained: Amount of barite is

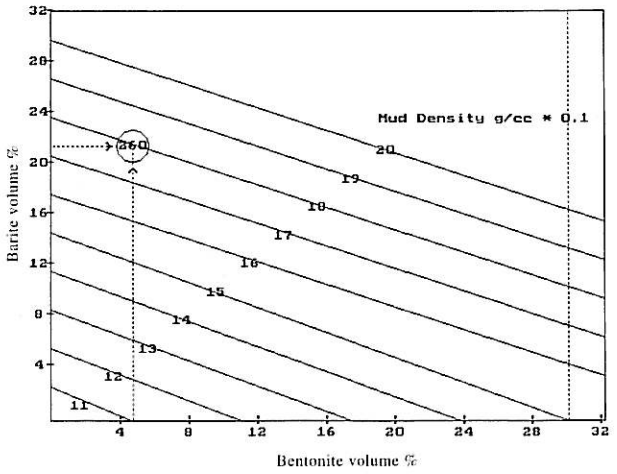


Fig. 2. Mud density as function of barite and bentonite volumes.

21.4% and amount of bentonite is still as previous i.e. 4.9%. from nomogram, the solid density is 3.963 g/cc. After viscosity measurement, the colloidity coefficient can be easily determined. Initial and final solid content are summarized in the Table 3.

Table 3. Optimum concentration of solid content

Initial mud density = 1.6 g/cc	Final mud density = 1.8 g/cc
Vsolid = 20%	Vsolid = 26.2%
Vclay = 4.9%	Vclay = 4.9%
Vbarite = 15.1%	Vbarite = 21.1%
K = 0.95	K = 0.955

CONCLUSIONS

1- A nomogram for quick evaluation of clay and drilling fluid quality has been successfully constructed.

2- Bentonite or any type of clay material having colloidity coefficient greater than 0.7 is recognized as good clay for drilling preparation purposes.

3- Drilling fluid contains any clay materials, having colloidal coefficient greater than (0.7), in range of (3.5 - 13%) is good mud with respect to the system stability and chemical additives consumption.

4- Content of clay materials greater than (13%) in the mud is not recommended because of low responsibility to chemical treatment and high consumption of dispersant. In contrary, a fractional volume of clay less than (3.5%) requires a greater quantity of filtration reducer and may result in the loss of system stability due to weighting materials sedimentation.

REFERENCES

[1] Carney, L.L., Skelly, W.G., and Gullickson, R., 1978. Quantitative determination of lignosulfonates in drilling fluids by ultraviolet adsorption analysis. Fall Meet, SPE, AIME, Oct. 2-6, SPE 3531 : 10 p.

[2] Chenevert, M.E., 1970. Shale alteration by water adsorption, *J. Petrol. Tech.* (Sept.). 1141-1148.

[3] Chilingar, G.V., and Coughlin, H., 1962. Easy and rapid method of determining mineralogical type of clays. Compass.

[4] Chilingarian, G.V., 1957. *Evaluation of clay for drilling fluids.* Compass.

[5] George, R.G., and Darley, H.C.H., 1980. *Composition and Properties of Oil Well Drilling Fluids.*, 4th. Edition., Gulf Publishing Company.

[6] Reznichenko, I.N., 1972. Preparation, treatment and cleaning of drilling fluids., Moscow, Nudra.

[7] *The Rheology of Oil-Well Drilling Fluids, API Bulletin*, 13d, 1st Ed., August 1980, American Petroleum Institute, Dallas.

[8] Van Olphen, H., 1977. *An Introduction to Clay Colloid Chemistry*, 2nd Ed. John Wiley & Sons, New York, p. 30.

[9] Weaver, C.E., and Pollard, L.D., 1973. *The Chemistry of Clay Minerals.* Elsevier, New York.

Petroleum Res. J. Vol. 10 (1998); P. 31-38, 7 Figs.

A ^{14}C-Radiotracer Study of the Hydrogenation of Ethyne on 0.3% $Pt/A1_2O_3$ (Europt-3)

Ezziddin A. Arafa*

التقفّى بالأثر الأشعاعي للكربون -14 في دراسة هدرجنة الإيثاين على سطح المحفز $Pt/A1_2O_3$

عز الدين أحمد عرفة

تمت دراسة إمتزاز أول أكسيد الكربون والمواد الهيدروكربونية الإيثان والإيثين بنظام مغلق عند درجة حرارة 293±2K باستخدام طريقة التقفى بالأثر الأشعاعي لعنصر ^{14}C، إمتزاز أول أكسيد الكربون بيّن السلوك المتوقع (التشبع عند ضغوط محددة) بينما إمتزاز الإيثان والإيثين تم بمرحلتين أولية وثانوية. وجد أو حوالي 30% من المواد الهيدروكربونية تبقى مُمتزة على سطح المحفز ولا يمكن سحبها بالخلخلة أو بتشبيع المحفز بالهيدروجين ولا بإجراء تفاعلات هدرجنة للإيثين.

تمت هدرجنة الإيثاين على سطح المحفز على مرحلتين، خلال المرحلة الأولى حسبت درجة التفاعل وكانت 1.73±0.06 بالنسبة للهيدروجين و 0.95±0.01- بالنسبة للإيثاين وثابت معدل التفاعل كان $2.4\pm0.1 \times 10^{-2}$ لكل دقيقة وبطاقة تنشيط تساوي 40.7±0.01كيلو جول لكل مول كما أن إنتقائية المحفز لتكوين الإيثين كانت 0.68.

أوضحت مراقبة سطح المحفز خلال عملية الإمتزاز أو تفاعلات هدرجنة الإيثاين أو الإيثين لا يمتز بالمواقع الحساسة لإمتزاز الإيثاين بينما الأخير يمتز بمواقع إمتزاز الأول. كما تبين أنه خلال تفاعل الهدرجنة يتم غمر سطح المحفز بالمواد الهيدركربونية خلال المراحل الأولى للتفاعل وأن المسلك الرئيسي لتكوين الإيثان (C_2H_6) يتم بالهدرجنة المباشرة للإيثاين.

تم تمييز عدد ثلاثة مواقع لهدرجنة (i) الإيثاين إلى الإيثين، (ii) الإيثاين إلى الإيثان (iii) والإيثين إلى الإيثان. أقترح أن سطح المحفز يمر بمرحلة إعادة بناء حيث يتم تكوين مواقع لإمتزاز الإيثاين والإيثين تحت ظروف إمتزاز المواد الهيدروكربونية وهدرجنتها.

Abstract: *Abstract Using the ^{14}C-radiotracer technique the adsorptions of carbon monoxide, ethene and ethyne have been studied in a static system at 293±2 K. ^{14}CO adsorption showed the Langmuir-type behaviour whilst the adsorption of both ^{14}C-ethene and ^{14}C-ethyne showed typical primary and secondary adsorption regions. A fraction ca.30% of the adsorbed hydrocarbon retained on the surface as strongly bound species and cannot be removed by evacuation, dihydrogen or ethyne hydrogenation treatments.*

Ethyne hydrogenation on Europt-3 proceeds in two distinct stages. During the first stage the reaction order is ca. 1.73±0.06 in dihydrogen and is ca. - 0.95±0.01 for ethyne. The reaction rate constant is ca. $2.4\pm0.1 \times 10^{-2}$ min-1 with an activation energy of ca. 40.7±0.3 k Jmol^{-1}. The initial selectivity for ethene formation is ca. 0.68.

Direct surface monitoring during the adsorption or hydrogenation reaction shows that ethene does not adsorb on the ethyne adsorption site whilst ethyne adsorb on ethene adsorption site. Evidence has been obtained to show that during the hydrogenation reaction, surface coverage by hydrocarbon progressively increases at the

*Tajoura Nuclear Research Centre, P.O. Box 30878, Tajoura, Libya.

commencement of the reaction and decreased linearly as the reaction proceeded.

The hydrogenation of ethyne in the presence of ^{14}C-ethene show that the yield of ethane from the hydrogenation of ethene constitute a very small fraction; the major route to ethane formation is by direct hydrogenation of ethyne. Three distinct types of surface sites are proposed as being responsible for the hydrogenation (i) ethyne to ethene; (ii) ethyne to ethane and (iii) ethene to ethane.

It is proposed that under the influence of hydrocarbon adsorption and hydrogenation reaction, the surface undergoes some reconstruction in which distinctive sites for the adsorption of ethyne and ethene are created.

INTRODUCTION

The hydrogenation of ethyne has been the subject of extensive investigations. It was first studied by Sheridan *et al.*[1,2] over pumice-supported metals, by Bond *et al.*[3,4] using alumina-supported metals and metal powders and more recently by Webb and his co-workers[5-9] on a range of supported Group VIII metal catalysts. The different aspects of the reaction have been reviewed by many workers[10-12].

Most of the early studies[1-4] were concentrated in evaluating the reaction kinetics and thermodynamic parameters to deduce the reaction mechanisms. The latter studies in particular, those employing the tracer technique[5-9], were carried out with the intention to sense the behaviour of the reactants during the adsorption and catalysis processes on clean and working catalysts in order to verify the deduced mechanisms.

It is generally accepted that the selectivity for ethene formation is associated with a thermodynamic factor which controls the relative surface coverage of ethyne and ethene (the same surface site being assumed to be involved in the adsorption of ethyne and ethene, i.e. depends on ΔH_{ads}.) and a mechanistic factor, which determines the extent to which the ethene is hydrogenated to ethane without undergoing intermediate desorption step (i.e. it is the catalyst property). The basis and extent to which the two factors operate either separately or together is not thoroughly clear, however, the reported studies indicate dependence on a number of variables in the system, such as, the activation energies of adsorbed and desorbed species[1-3], hydrocarbon: dihydrogen ratio[4], catalyst preparation and pretreatments[5-9] and type of support[12].

This paper is an extension to our previously reported studies[8] on ethyne hydrogenation over supported Group VIII metal catalysts and reports the adsorption of carbon monoxide, ethene and ethyne hydrogenation over the standard reference EUROPT-3, (Pt/Al_2O_3) catalyst[13].

EXPERIMENTAL

Catalyst

The catalyst used in this study is a standard catalyst containing 0.3% (w/w) Pt/Al_2O_3-0.82%Cl designated by the Council of Europe Catalysis Group as EUROPT-3 and has the industrial code KETJEN-CK303. The catalyst has a BET surface area of 184 m^2g^{-1} and pore volume of 0.49 cm_3g^{-1} [13].

Materials

^{14}C-carbon monoxide was prepared by the reduction of ^{14}C-carbon dioxide using metallic zinc as described elsewhere[5]. ^{14}C-ethene and ^{14}C-ethyne were supplied by the Radiochemical Centre, Amersham, of specific activities 5.8 mCi $mmol^{-1}$ and 1.08 mCi $mmol^{-1}$ respectively. Before use, each ^{14}C-labelled gas was diluted with the respective non-radioactive gas (B.O.C. Ltd) to give specific count rates of ca. 400,000 counts min^{-1} Po^{-}.

Apparatus

The adsorption and hydrogenation measurements were made in a reaction vessel of a similar design to that described earlier[5]. The reaction vessel (416 cm^3) was fitted with two inter-calibrated Geiger-Muller (GM) counters (Mullard MX168/01) to permit direct observation of the adsorbed species, during subsequent treatments and hydrogenation of hydrocarbons. The apparatus was maintained at a pressure of 0.0133 Pa by means of mercury diffusion pump backed by a rotary oil pump. Pressures in the reaction vessel were measured using a calibrated pressure transducer (S.E.Type SE/V/10D) capable of

accurately recording pressure change as low as 1.33 Pa.

To faciliate analysis of the gas phase on contact with the catalyst surface during the adsorption or subsequent surface processes, the reaction vessel was connected to a gas-sampling system which was coupled to a combined gas chromatograph-proportional counter. Analysis was performed using a 1.0 m (2.0 mm, i.d.) stainless-steel column packed with 40-60 mesh activated silica (Aerosil, Degussa Ltd). The column was operated at 313 K with helium (Air Products Ltd) as the carrier gas at a flow rate of 60 cm^3 min^{-1}. On elution from the column, the eluant was mixed with the required amount of methane (Air Products Ltd) before it entered the gas proportional counter.

Procedure

For catalyst reduction, the catalyst (typically 0.30±0.05g) in a finely divided form (100 B.S.S. mesh) was spread uniformly in a glass boat-shaped container and positioned in a part of the reaction vessel which was surrounded by an electric furnace. Dihydrogen was introduced to the catalyst at a flow rate of 30 cm^3min^{-1}, the temperature of the catalyst was raised at 5 $Kmin^{-1}$ to 523 K and maintained at this temperature for 2 h. The reaction vessel was then evacuated at 523 K for 30 min and the catalyst cooled *in vacuo* to ambient temperature.

A sample of Europt-3 was calcined in air at 773 K for 28 h, reduced in flowing dihydrogen at 673 K for 4 h and was then evacuated at 673 K for 30 min before being cooled to ambient temperature.

Adsorption of ^{14}C-carbon monoxide and ^{14}C-hydrocarbons was investigated by admitting small aliquots of the relavent gas to the reaction vessel, determining surface and gas-phase count rates after ~10 min equilibration (each determination is an average of triplicate measurements).

In the hydrogenation of ethyne a premixed 1:3 ethyne/dihydrogen mixture ratio at a total pressure of 6.67 kPa was admitted to the reaction vessel. The reaction was followed by the pressure fall recorded by the pressure transducer, samples being extracted at any desired pressure fall (% conversion) for analysis. All the adsorption and hydrogenation measurements were made at 293±2 K.

RESULTS AND DISCUSSION

Adsorption of ^{14}C-Carbon Monoxide

The adsorption isotherms obtained by admitting successive aliquots of ^{14}C-carbon monoxide to freshly reduced, deactivated (steady state catalyst) and calcined catalysts are shown in Figure 1. The adsorption on a freshly reduced catalyst showed the expected behaviour, the surface count rate increased linearly with increasing gas pressure until a plateau region was obtained, characteristic of Langmuir-type adsorption isotherm. The plateau region however, showed a slight positive gradient, such behaviour has been observed on a silica supported platinum catalyst (EUROPT-1)[8] and on oxidised copper surfaces[14]. The extent of ^{14}CO adsorption on a steady state catalyst is reduced remarkably to ca. 30% of that obtained on freshly reduced catalysts. This behaviour has also been encountered on supported Ni, Pd, Ir and Rd catalysts[5,7] and interpreted as due to adsorption of carbon monoxide in a linear mode on single metal sites left vacant following the dissociative adsorption of ethyne.

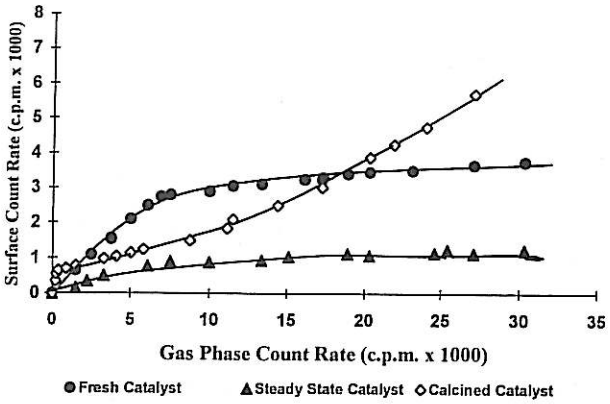


Fig. 1. Adsorption of ^{14}C-carbon monoxide on europt-3 at 293±2 K.

The adsorption of ^{14}CO on a freshly reduced calcined sample of the catalyst showed no plateau region as the gas pressure was increased. This behaviour suggests that treatment of Europt-3 in oxygen at 673 K tend to lower its dispersion and severely oxidize platinium atoms.

The effects of various treatments on the adsorbed carbon monoxide were also investigated, and the results are summarised in Figure 2. From these it can be seen that ca. 23% of the adsorbed ^{14}CO can be removed by evacuation and a further ca. 30% fraction can only be removed by cycles of dihydrogen - evacuation - ethyne hydrogenation treatments, however, ca. 47% of the adsorbed ^{14}CO is retained by the catalyst as strongly bound species. Kramer *et al.*[15] from their CO temperature programed desorption studies on Pt/SiO^2 catalyst identified such tightly bound CO species to be CO adsorbed at the phase boundary platinum/support in a slow adsorption process which may correspond to the primary adsorbed species of the adsorption isotherm (Fig.1) and in agreement with our findings such species can only be removed by cycles of oxidation-reduction at ~750 K.

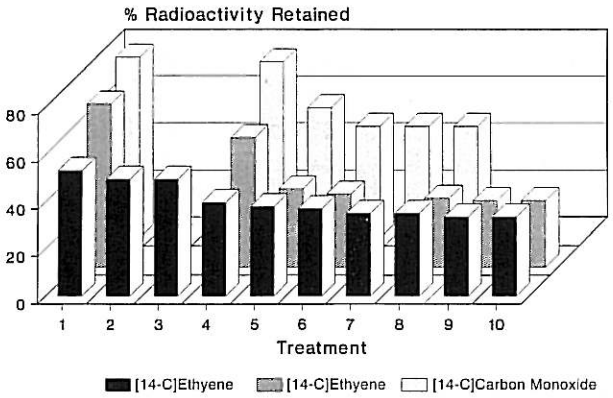


Fig. 2. Variations in surface count rates when a precovered surface was subjected to various treatments at 293±2 K.: 1.evacuation (30 min); 2.ethyne hydrogenation; 3.evacuation (30 min); 4.dihydrogen (13.33 k.pa for 15 h); 5.ethyne hydrogenation; 6.ethyne hydrogenation; 7.dihydrogen (13.33 k. pa. for 15 h); 8.ethyne hydrogenation; 9.dihydrogen (13.33 k. pa. for 15 h); 10.ethyne hydrogenation.

Adsorption of ^{14}C-Ethene and ^{14}C-Ethyne

The adsorption isotherms of ^{14}C-ethyne and ^{14}C-ethene on freshly reduced samples of Europt-3 catalysts are shown in Figures 3 and 4 respectively. They are of a similar form to the isotherms observed previously on Pt/SiO^2 (Europt-1) catalyst[8] and over the other supported Group VIII metals[5-7], showing a non-linear primary region and a linear secondary region. The extent of adsorption in the secondary region continued to increase with increasing adsorbate pressure, no plateau was reached even though gas pressures >0.7 Kp were used. When samples of the catalyst were precovered with C_2H_x species or run to their steady-state by sucssessive hydrogenations using 1:3 ethyne:dihydrogen mixtures and followed by ^{14}C-hydrocarbon adsorption, only the secondary adsorption region is observed (Figs. 3 and 4). Comparision of the amounts of ^{14}C-ethyne adsorbed on the primary region of a freshly reduced catalyst with the corresponding value for the adsorption of ^{14}C-carbon monoxide shows that the ratio of ethyne to carbon monoxide molecules on the surface is ca. 0.7:1.0 while the ratio of ethene to carbon monoxide is ca.0.2:1.0. The same ratios were also found to hold on steady-state catalysts. Assuming as generally accepted that ethyne and ethene adsorption occur as dissociative species, these results suggest that ~30% of the surface, for geometric reasons, not available for ethyne adsorption and ~80% of the surface sites for the same reason are unable to accomodate ethene molecules. These findings with the observations that no adsorption of ethene was observed to occur on ethyne precovered surfaces, whilst on ethene precovered surfaces, subsequent adsorption of ethyne resulted in a displacement of ca.50% of the pre-adsorbed ethene, clearly indicate that ethene adsorption occur on distinctive sites wherease ethyne adsorption can take place on more than site type. No ethene was ever observed as a self-hydrogenation product from the adsorption of ethyne.

The gas-phase hydrocarbon in contact with the surface during the build-up of the ^{14}C-ethyne and ^{14}C-ethene adsorption isotherm was analysed by radio-gas chromatography. This showed that during the build-up of the primary region (up to the turning point in the adsorption isotherm) the only hydrocarbon in contact with the surface was ethane.

The effect of subsequent treatments on ^{14}C-ethyne or ^{14}C-ethene precovered surfaces is shown in Figure 2. Note that about 70% of the adsorbed ^{14}C-hydrocarbons were effectively be removed by cycles of evacuation-ethyne hydrogenation-dihydrogen treatments at ambient temperature and the remaining ~30% of the ^{14}C-hydrocarbon species retained strongly adsorbed on the surface and can completely be removed by reduction in flowing dihydrogen cycles at 523 K.

Ethyne Hydrogenation Reactions

For the hydrogenation of ethyne at 1.67 kPa with dihydrogen at 5.0 kPa over 2.0±0.5g catalysts, plots of pressure against time curves showed that the reaction to occur in two distinct stages, the onset of the second stage being accompanied by an increase in rate at a pressure fall of ca. 1.67±0.027 kPa and ascribed to ethene hydrogenation in availability of dihydrogen[6]. Up to this acceleration point, the reaction order is ca. 1.73±0.06 in dihydrogen and ca. - 0.95±0.01 for ethyne with a rate constant of ca. 2.4 0.1 x 10^{-2} min^{-1} and an activation energy of ca.40.7± 0.3 kJ mol^{1}.

When series of ethyne hydrogenation reactions were performed over the same catalyst sample, it was observed that from reaction to reaction the activity progressively decreased until a steady-state activity was attained. Both the first and second stages of ethyne hydrogenation were deactivated by similar amounts. Treatment of a freshly reduced catalyst with ethyne alone for extended periods, before carrying out the hydrogenation reactions, did not have any significant effect on the deactivation process. From this and similar observations on Group VIII metal catalysts[5-9], it can be suggested that the deactivation does not simply arise from a build-up of carbidic or other hydrogen defficient carbonaceous residues on the surface, resulting from the dissociative adsorption of ethyne, but rather from a process involving the interaction of ethyne with dihydrogen on the catalyst surface. Such a thought has been previously coined by Thomson and Webb[12] in which they proposed that the hydrogenation on metals should be interperated as hydrogen transfer between an adsorbed hydrogen-defficient hydrocarbon species, M-CxHy, and adsorbed alkene and alkyne, rather than the direct addition of hydrogen to an associatively adsorbed hydrocarbon. The deactivation process did not have any effect upon the acceleration point of the reaction, although the selectivity, S, which defined as: $S = P_{ethene} / (P_{ethene} + P_{ethane})$ increased by ca. 6% as the catalyst run to its steady-state activity. The average selectivity for ethene formation over Europt-3 is ca. 0.677±1.8%.

Regeneration of Europt-3 can be achieved by heating at 573 K in flowing pure dihydrogen (30 cm^3 min^{-1}) for 2 h and evacuation at 573 K for 30 min (Figs 3 and 4).

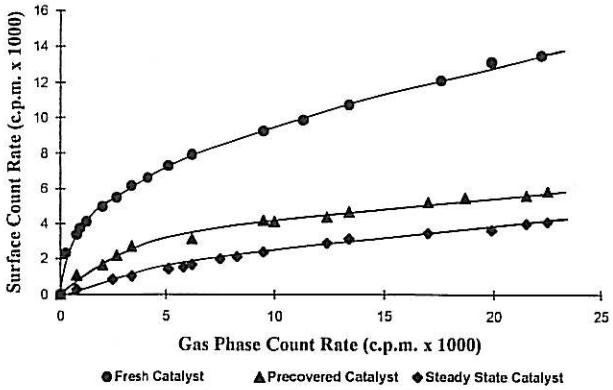


Fig. 3. Adsorption of ^{14}C-ethyne on europt-3 at 293±2 K.

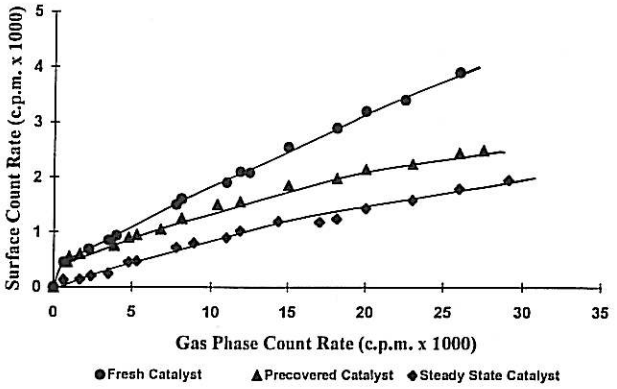


Fig. 4. Adsorption of ^{14}C-ethyne on europt-3 at 293±2 K.

Ethyne hydrogenation on clean and steady-state samples of Europt-3 was followed by monitoring the surface radioactivity during the course of the reaction. The results presented in Figure 5, showed that when a 1:3 ^{14}C-ethyne:dihydrogen mixture reacted on clean or steady-state catalysts, the surface radioactivity representing the adsorbed ^{14}C-species increased almost sharply at the comencement of the reaction and then decreased linearly as the reaction proceeded, this extent is more pronounced on clean catalyst in comparision on deactivated catalyst. This implying the formation of surface monolayer coverage on the freshly reduced surface and the adsorption of ^{14}C-species on the metal sites made available following ethyne hydrogenation on the steady-state catalyst.

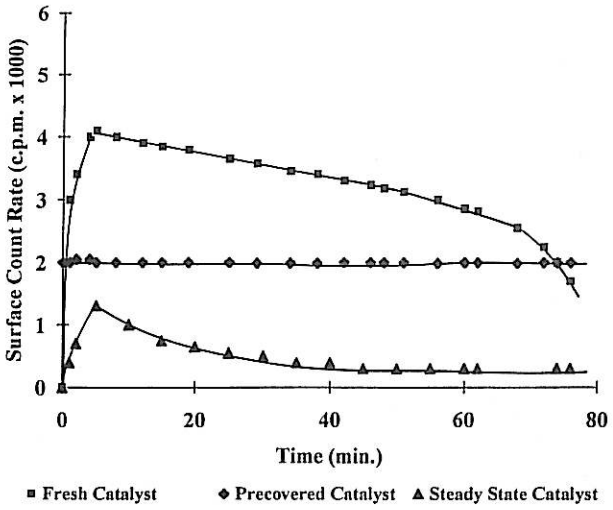


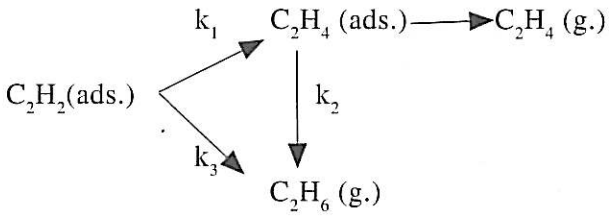
Fig. 5. Variations in surface count rate during the hydrogenation of 1.67 k. pa. ^{14}C-ethyne with 4.99 k. pa. dihydrogen on europt-3 at 293±2 K.

When the catalyst was precovered with pressures of ^{14}C-ethyne capable of building up the primary region of the adsorption isotherm and followed by 1:3 ^{12}C-ethyne:dihydrogen mixture reaction on the same catalyst, the surface radioactivity remained unchanged during the course of the reaction (Fig. 5). This is another evidence to support the suggestion made earlier from the ^{14}C-hydrocarbon adsorption behaviour that, catalysis of ethyne hydrogenation takes place on the secondary adsorption region.

Hydrogenation of 12C-Ethyne + ^{14}C-Ethene Mixtures

In order to gain some insight into the mechanism of the selective hydrogenation of ethyne over Europt-3, a series of reactions were carried out on steady-state catalysts using 1:3, ethyne:dihydrogen and varied aliquots of ^{14}C-ethene which were added to the reaction mixture before admission to the reaction vessel. The amount of radioactivity in the individual reaction products was determined by radio-gas chromatography. The results are shown in Table 1. From these, two interesting features emerge, first, the amount of ^{14}C-ethane constitutes a small proportion of the total ethane yield relative to the amount expected from the amounts of added ^{14}C-ethene and the ^{12}C-ethene present in the reaction vesel. This suggests that only minute amounts of ethene undergo readsorption and further hydrogenated to ethane until all of the ethyne has hydrogenated. Secondly, the yield of ^{14}C-ethane increased linearly as the reaction proceeded and was directly proportional to the amount of ^{14}C-ethene added to the reaction mixture.

Using the data of Table 1 and the possible routes for the hydrogenation of ethyne presented below:



the relative values of the rate constants were calculated according to the procedure of Brendt *et al.*[7] and found to equal: k_1= 0.071±4% , k_2= 0.009±3.3% and k_3= 0.163±4% at 293±2 K.

CONCLUSIONS

The obtained results of the adsorption of carbon monoxide, ethyne and ethene and the hydrogenation of ethyne on Europt-3 are of similar characteristics to those shown by Europt-1 and other supported Group VIII metals[5-9]. The adsorptions of ^{14}C-hydrocarbons occur in two distinct stages; a non-linear primary region followed by a linear secondary region and ethyne hydrogenation is associated with hydrocarbon species adsorbed on the secondary region.

The results of the ^{14}C-hydrocarbon adsorptions together with the ^{14}C-ethene tracer studies show the presence of separate surface sites for the hydrogenation of ethyne to ethene, the hydrogenation of ethyne to ethane and the hydrogenation of ethene to ethane. This consistent with a mechanism previously proposed by Webb and co-workers[7,8] for the hydrogenation of ethyne over supported Group VIII metal catalysts as shown in Figure 6.

Although the precise population of these different surface site types is difficult to assess, however, from the extent of ^{14}C-carbon monoxide and hydrocarbons adsorptions and using the rate constants presented above they can roughly be estimated to represent, Type I sites = 29.2%,

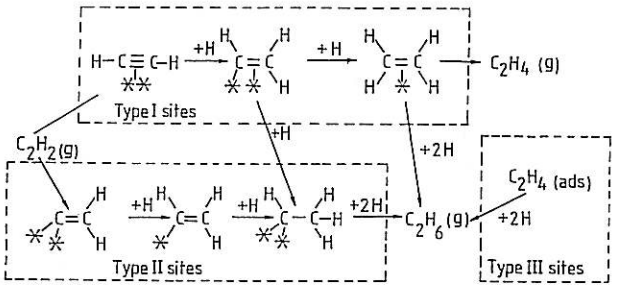


Fig. 6. Surface site types responsible for ethyne hydrogenation on supported metal catalysts.

Type II sites = 67.1% and Type III sites = 3.7%. Collectively, the results of this study concludes that Europt-3 catalyst shows a high thermodynamic selectivity but a low mechanistic selectivity.

From the ^{14}C-adsorption studies and ethyne hydrogenation reactions over Europt-3 and on the other supported Group VIII metal catalysts studied[5-9], we conclude that during the adsorption of hydrocarbons or ethyne hydrogenation, a rearrangement of the surface occurs resulting in the freeing of metal sites on the surface. The precise origins of such rearrangement cannot fully be established from the present studies. It could, however, arise due to the movement of some metal atoms through the hydrocarbonaceous primary layer, under the influence of the hydrogenation reaction or adsorbed hydrocarbons as predicted in Figure 7. Such phenomenon has been observed in the hydogenation of hydrocarbons on supported Ni and Pt catalysts and termed corrosive chemisorption[16,17].

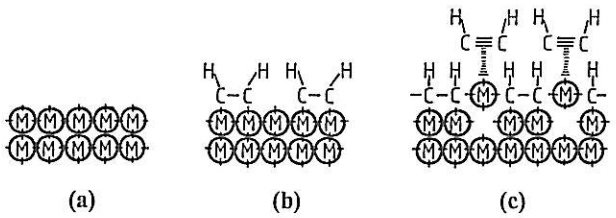


Fig. 7. Model for surface reconstruction as a result of adsorption or catalysis of hydrocarbons on supported catalysts. (a) clean surface; (b) hydrocarbon covered surface; (c) reconstructed surface.

According to such surface rearrangement model, the deactivation of the Group VIII metal catalysts to a steady-state activity could be interpreted as the establishing of a steady-state concentration of active metal sites by migration of individual metal atoms into the hydrocarbanaceous layer adsorbed on the primary region, these metal atoms being responsible for the secondary adsorption process and catalysis. The presence of the carbonaceous overlayer causes a modification of the surface orbitals to the extent that distinct sites for the adsorption of ethyne and ethene, as -bonded complexes are created.

Table 1. Variation of product composition (in pascal) as a function of extent of hydrogen uptake during the hydrogenation of 12C-ethyne in the presence of varied amounts of added 14C-ethene at 293(2 K

Conversion (%)	$P(^{12}C_2H_4)$	$P(^{12}C_2H_6)$ *(Total)*	$P(^{12}C_2H_6)$ *(Direct)*	$P(^{14}C_2H_6)$
		^{14}C-ethene = 133.3 Pa		
20.0	184	43	39	2.7
41.9	335	109	101	2.9
75.9	536	165	151	3.3
91.2	661	252	228	4.8
		^{14}C-ethene = 266.6 Pa		
13.1	128	21	17	7.2
45.0	372	48	36	8.3
93.0	528	212	188	10.9
113.7	575	247	221	11.9
		^{14}C-ethene = 666.6 Pa		
10.9	97	21	19	13.2
40.1	235	129	123	17.3
65.4	413	179	167	17.6
105.6	543	279	257	24.4

REFERENCES

[1] Sheridan, J., 1944. *J. Chem. Soc.*, 373-476.
[2] Sheridan, J. and Reid, W.D., 1952. *J. Chem. Soc.*, 2962-2964.
[3] Bond, G.C. and Wells, P.B., 1965. *J. Catal.*, **4**, 211-215.
[4] Bond, G.C., Webb, G. and Wells, P.B., 1968. *J. Catal.*, **12**, 157-165..
[5] Al-Ammar, A.S. and Webb, G., 1978, *J. Chem. Soc. Faraday Trans.I*, **74**, 195-205, 657-664.
[6] Al-Ammar, A.S. and Webb, G., 1979. *J. Chem. Soc. Faraday Trans.I*, **75**. 1900-1911.
[7] Berndt, G.F., Thomson, S.J. and Webb, G., 1983. *J. Chem. Soc. Faraday Trans.I*, **79**, 195-207.
[8] Arafa, E.A. and Webb, G. 1993. *Catal. Today*, **17**, 411-418.

[9] Kuhnen, N.C., Thomson, S.J. and Webb, G., 1983. *J. Chem. Soc. Faraday Trans. I*, **79**, 2195-2210.
[10] Bond, G.C. and Wells, P.B., 1963. *Adv. Catalysis*, **15**, 91-226.
[11] Wells, P.B., 1972. Surfaces and Defect Properties of Solids, Specialist Periodical Reports. *Royal Chem. Soc. London*, **1**, 24.
[12] Webb, G., 1978. Catalytic hydrogenation. In: C.H. Bamford, and C.F. Tipper, (eds). *Comperhensive Chemical Kinetics*, Academic Press, **20**, 1-114.
[13] Bickle, G.M., Biswas, J. and Do, D.D., 1988. *Appl. Catal.*, **36**, 259-265.
[14] Kinnaird, S., Webb, G. and Chinchen, G.C., 1987. *J. Chem. Soc., Faraday Trans. I*, **83**, 3399-3413.
[15] Kramer, R., Fischbacher, M. and Gruber, H.L., 1988. *Appl. Catalysis*, **42**, 337-350.
[16] Jackson, S.D., Thomson, S.J. and Webb, G., 1981. *J. Catal.* **70**, 249-263.
[17] Burwell, R.L., Kung, H.H. and Pellet, R.J., 1976. *Structure Sensitivity and Selectivities in Competitive Reactions, Bond, G.C.. In:* Wells, P.B and F.C. Tompkins. (eds.) Proc. 6th Int. Congr. Catal., *Chem. Soc., London*, **1**, 108-116.

Petroleum Res. J. Vol. 10 (1998); P. 39-44, 3 Figs.

Thermal Stability Study of Ras Lanuf Jet Fuel by NMR-Spectroscopy and Gas Chromatography Mass Spectrometry

Gamil Alhakimi, Saleh Gebril,
Ibrahim Rajab, Ibrahim Altijani*

دراسةالثبات الحراري لوقود الطائرات المنتج بشركة رأس لانوف بواسطة جهازي الرنين النووي والكروماتوغرافية وتحديد الكتلة

جميل الحكيمي و صالح جبريل و إبراهيم رجب و إبراهيم التيجاني

تم دراسة الثبات الحراري لوقود الطائرات المنتج في شركة رأس لانوف لتصنيع النفط والغاز بواسطة جهاز الرنين النووي المغناطيسي والكروماتوغرافية وتحديد الكتلة. حيث تم تسخين الوقود عند درجات حرارة مختلفة 360، 380، 400، 240، درجة مئوية، كما تم تحديد الكم الحجمي لكل من المركبات الأورماتية والأليفياتية بواسطة جهاز الرنين المنغاطيسي ولوحظ أن بداية تكون المواد الولوفينية والأروماتية في درجات الحرارة العالية. كما لوحظ إرتفاع مفاجئ في كمية المواد الأروماتية في C_{12}، C_{11} يواكبه إنخفاض في كمية المواد الأليفاتية عند درجات الحرارة العالية (420، 440 درجة مئوية). أما التعرف النوعي على المواد الجديدة الناتجة فقد تم بواسطة جهار الكروماتوغرافية وتحديد الكتلة. وكانت بداية تكون مادة الكربون الصلب عند درجة حرارة 420 مئوية، وارتفعت هذه الكمية إلى 19.5% من الوزن الكلي عند درجة حرارة 440 مئوية.

Abstract: *Abstract The thermal stability of jet fuel produced by Ras Lanuf refinery was studied by nuclear magnetic resonance-spectroscopy (n.m.r.) and gas chromatography mass spectrometry (g.c-m.s.). The fuel was thermally stressed for 3 hours at different temperatures 360, 380,400.420 and 440 °C. The vol% of aromatics, olefins and paraffins was calculated by proton n.m.r. spectroscopy. The buildup of olefinic compounds started at 380 °C. GC analysis indicated that the formation of olefins and aromatics at high temperatures was accompanied by a decrease in C_{11} and C_{12} aliphatic fractions. Rapid increase of aromatics content was also observed at high temperatures (420-440 °C). Identification of the new formed compounds was carried out by g.c-m.s. The formation of solid carbonaceous deposits was firstly observed at 420 °C. Its content reached 19.5 wt% at 440 °C.*

INTRODUCTION

The development of new high speed aircraft generation required a fuel with high thermal stability. The fuel for such aircrafts would have to withstand temperatures in the range of 400-500 °C for several hours and the pyrolytic degradation of the jet fuel at this speed may be much more important than autoxidation. The possibility of the fuel pyrolysing and forming solid carbonaceous deposits in the fuel delivery system is of particular concern because of deposition of such materials in fuel lines or burner nozzles could lead to catastrophe. Jet fuels are mixtures with a huge number of hydrocarbons that became an extraordinarily complex chemical composition following thermal stressing at elevated temperatures. The distribution of molecular

*Ras Lanuf Oil & Gas Processing Co.

species broadens as cracking and transformation reactions produce a myriad of aliphatic and aromatic molecules of varying structures and molecular weights[1].

Conventional jet fuels are limited to maximum heating temperature of about 300 °C. Thermal oxidation stability of jet fuels at 100 to 300 °C in presence of oxygen has been researched for several decades[2-8]. For the development of fuel that will resist degradation by thermal stressing, the scientist should understand how the molecular structure of the fuel affects the thermal stability and what the molecular mechanisms that lead to the formation and accumulation of carbonaceous solids are. Many studies of fuel thermal stability were carried out. The principal indication of thermal instability was found to be the amount of solid carbonaceous deposit that forms during thermal stressing in a closed reactor[9]. The other important indicator was the formation of gaseous products. The change of the jet fuel composition can be followed by different methods. N.M.R-spectroscopy has been widely used to characterize petroleum oils and fractions[10-15]. The use of n.m.r. spectroscopy offers distinct advantages over other spectroscopic methods since it can be recorded in relatively short times, and it provides detailed compositional characteristics of the oil fraction that are unobtainable by other methods. The g.c-m.s technique has also contributed greatly to the analysis of various petroleum fractions[16,17].

In this work, the change of the chemical composition of jet fuel at different temperatures (360, 380, 400 and 420 °C) was followed by means of n.m.r. spectroscopy and g.c-m.s. The structure parameters obtained by the spectra are discussed and the composition change of the jet fuel at different temperatures is presented. The new formed compounds are separated and identified by g.c-m.s. This paper represents the first step of a research programme in the RASCO laboratory for investigating the compositional factors that affect the thermal stability of jet fuel.

EXPERIMENTAL

The jet fuel fraction was received from Ras Lanuf refinery (distillation temperature 150-204 °C). The fuel was heated for 3 hours in a stainless steel autoclave designed in the RASCO workshop. N.M.R. spectra was obtained by Bruker 100 Mhz spectrometer in 5 ml probe. Tetramethyl silane was used as an internal standard and deuterated chloroform as a solvent.

The integration and treatment of the obtained spectra was carried out on the Bruker data station with the WINNMR program. For g.c-m.s analysis a UNICAM series 610 Automass instrument, equipped with a 105 m Fison DB-1 (d=0.25 mm) capillary column, operating temperature programmed (150 °C for 25 min, rate 5 °C/min up to 300 °C with helium as a carrier gas. GC analysis had been performed using Carlo Erba Instrument 4100 equipped with 105 m Fison DB=1 (d=0.25mm) capillary column, operating temperature programmed (150 °C for 25 min, rate 5 °C/min up 300 °C with helium as a carrier gas.

RESULTS AND DISCUSSION

Theory of the n.m.r calculation:

The n.m.r. method is based on calculating the relative number of carbon atoms, classified as aromatics, paraffinis, or olefins in jet fuel from n.m.r. integral spectrum. The calculation of the composition of aromatics, paraffins and olefins by volume is given by the following equations[18, 19]:

$$\text{Aromatics, vol \%} = \frac{1.279.\,(A + C/3)}{1.279.\,(A + C/3) + (D - 2B + E/2 + F/3) + 2.5.\,B} \times 100 \quad (1)$$

$$\text{Paraffins, vol \%} = \frac{(D - 2B + E/2 + F/3)}{1.279.\,(A + C/3) + (D - 2B + E/2 + F/3) + 2.5.\,B} \times 100 \quad (2)$$

$$\text{Olefins, vol \%} = \frac{2.5.\,B}{1.279.\,(A + C/3) + (D - 2B + E/2 + F/3) + 2.5.\,B} \times 100 \quad (3)$$

A = aromatic carbons

B = olefinic carbons

C = CH2 and CH3 substituted to aromatic ring

D = aliphatic tertiary C-atoms

E = aliphatic methylene groups

F = aliphatic methyl groups

Some carbon atoms go uncounted for because they are completely substituted and give no n.m.r signal. Other carbons are erroneously counted as belonging to a given hydrocarbon class. Their protons resonate in the regions of n.m.r. spectrum where other hydrocarbon types normally appear. The densities of the light paraffins and aromatics are different, therefore, correction factors for these effects are carried out. The densities of aromatic compounds are significantly greater than paraffins. The aromatic terms in equation (1) through (3) need to be multiplied by a constant to correct the density differences. For these purposes, a quantitative determination of individual compounds in kerosene was carried out by gas chromatography. The weighted average density for each hydrocarbon class was calculated by the following equation[19]:

$$\text{weighted average density} = \frac{\Sigma\,[\,\text{vol}\%_{(i)}]\,[\text{density}_{(i)}]}{\Sigma\,[\,\text{vol}\%_{(i)}]} \quad (4)$$

The weighted average density for aromatics was found to be 0.8662 g/ml and for paraffins 0.7592g/ml. The aromatic term (A+C/3) must, therefore, be multiplied by 0.8765 to correct the density differences.

In the n.m.r. spectroscopy, the full substituted carbon atoms give no signal. Correction factor for this phenomena was also calculated for individual compounds in kerosene fraction. The following equation was applied[19]:

$$\text{weighted average ratio (carbon counted/carbon uncounted)} = \frac{\Sigma\,[\,\text{vol}\%]\,(i)\ \dfrac{\text{no. carbon counted (i)}}{\text{no.carbon uncounted (i)}}}{\Sigma\,[\,\text{vol}\%(i)]} \quad (5)$$

The correction factor for aromatics in kerosene fraction was found to be 0.6843. The aromatic term in the equations mentioned above (1,2 and 3) must be multiplied by 1.46. That means the overall constant to multiply the aromatic term with is 1.2796.

Correction factors of weighted average density and weighted ratio (carbon counted/carbon uncounted) for olefins were also calculated. The weighted average density for olefins was found to be 1.1704 and the weighted ratio (carbon counted/carbon uncounted) 2.14. The overall constant to be applied to the olefinic term is 2.5.

For paraffins, no density correction was necessary because the aromatics and the olefins were normalized to the paraffins density. Weighted average ratio for paraffins was calculated only. Its value was 1.

n.m.r. analysis:

The proton n.m.r. spectra for the base kerosene fractions obtained from the RASCO refinery and for the thermally stressed kerosene samples are indicated in Figures (1-3) and Table 1. The integral values for the regions were obtained from the spectra and were calculated by the above mentioned equations. The n.m.r. spectra were divided into the regions of interest based upon the chemical shifts of specific proton types. These areas are illustrated in Table 2.

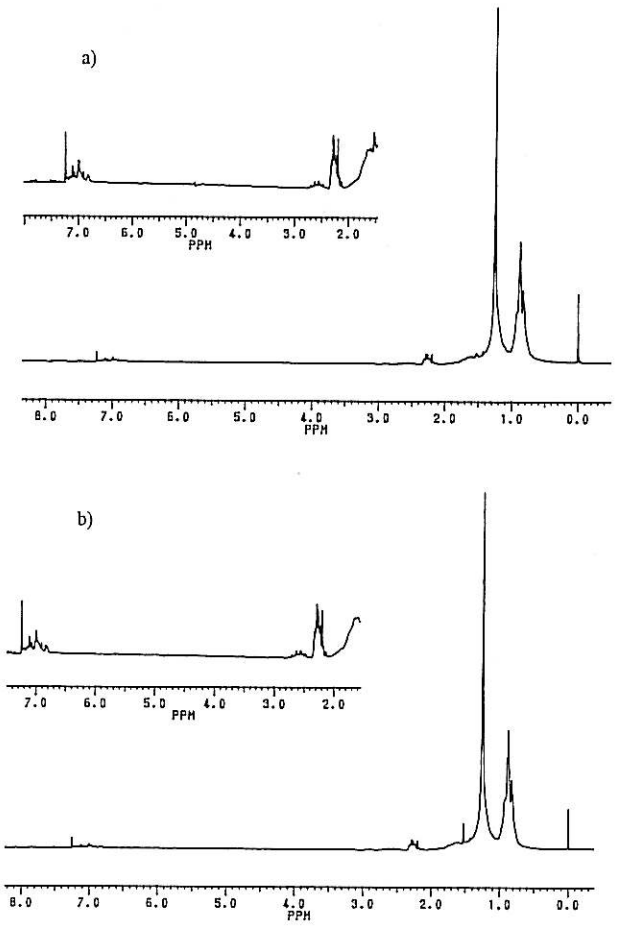


Fig. 1. ^{1}H-NMR spectra of a) base kerosene without heating and b) for kerosene heated for 3h at 360 °C, $CDCl_3$ as solvent and TMS as standard.

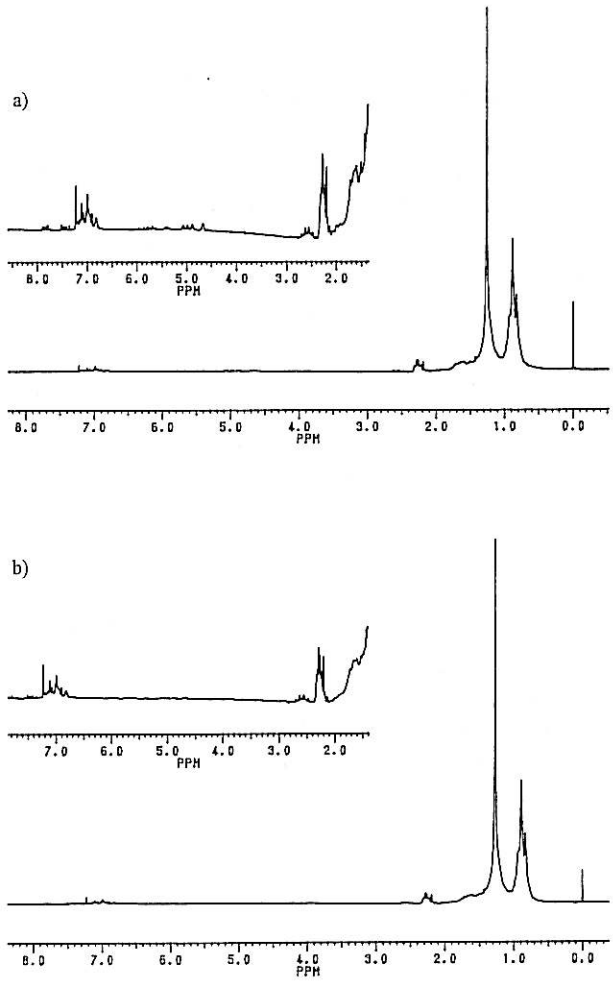


Fig. 2. ^{1}H-NMR spectra of a) thermally stressed kerosene at 400 °C and b) thermally stessed kerosine at 380 °C, $CDC1_3$ as solvent and TMS as standard.

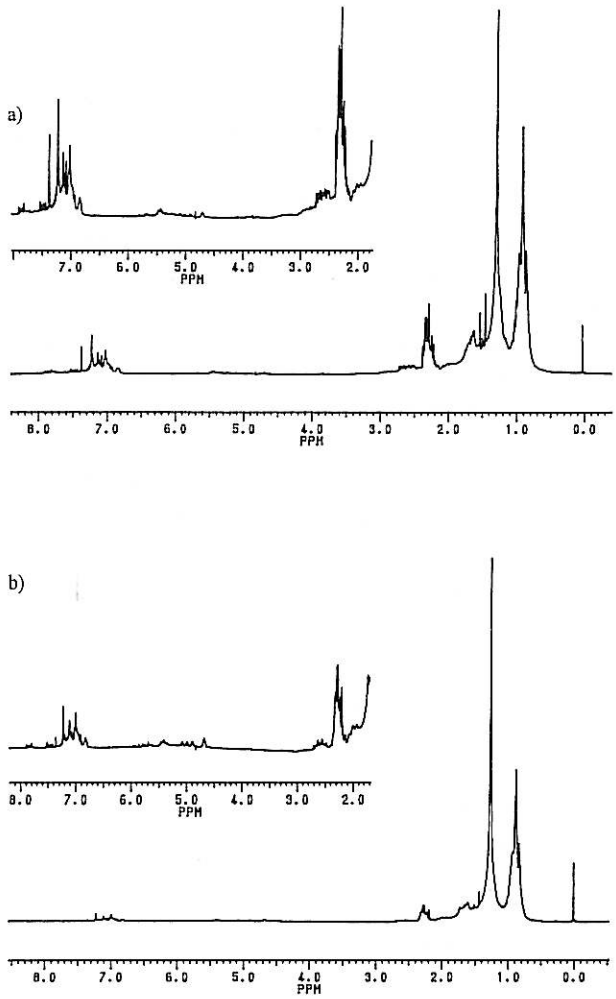


Fig. 3. ^{1}H-NMR spectra of a) thermally stressed kerosene at 440 °C and b) thermally stressed kerosene at 420 °C, $CDC1_3$ as solvent and TMS as standard.

Table 1: Properties of the RASCO base kerosene

Specific gravity	0.7855
Density g/ml	0.7853
API gravity	48.64
Freezing point, °C	-55
total sulphur, wt%	0.0023
Smoke point, mm	29

Table 2: Proton n.m.r assignments for functional groups of interest in kerosene[21,22]

Chemical shift region (ppm)	Proton type
0.6 to 1.0	hydrogen atoms of CH_3 in aliphatics and CH_3 in γposition and more distance to aromatic ring
1.0 to 1.5	CH in aliphatics and CH, CH_3 in β position to aromatic ring
1.5 to 2.151.5	CH in aliphatics and CH_2 to double bounds
2.15 to 3.0	CH, CH_2 and CH_3 in α-position to aromatic ring
4.5 to 6.0	CH to olefins
6.6 to 8.0	CH to aromatic ring

The increase of temperature up to 360 °C showed no change in the kerosene composition. By temperature at 380 °C a value of 2.8 vol% of olefinic compounds was obtained. At this temperature, formation of solid carbonaceous deposits was not observed. The colour of the kerosene remained unchanged. Table 3 shows that at high temperatures (T-400-440 °C), the paraffinic carbons are extensively converted to olefins and aromatics. The colour of the kerosene becomes yellow at these temperatures. Building up of carbonaceous solids started at 420 °C and the olefins and aromatics quantities go up to 14.9 vol% and 12.9 vol% respectively. A rapid increasing in the formation of carbonaceous solids was observed at 440 °C. At this temperature, 19.5 wt% carbonaceous solid was found. The aromatic content was increased to 57.4 vol%. The n.m.r. results indicated that the primary pathways to form carbonaceous solid are firstly, formation of olefins and secondly, cyclization to aromatics. This conclusion is derivable from the n.m.r. results shown in Table 3.

Table 3: Composition of thermally treated jet fuel by n.m.r spectroscopy and carbonaceous solid formation

Tempera-ture/°C	Aliphatics (vol%)	Olefinics (vol%)	Aromatics (vol%)	Carbon-aceous solid (wt%)
150-204	88.32	—	11.58	0.00
360	88.17	—	11.83	0.00
380	85.3	2.8	11.9	0.00
400	84.16	3.84	12	0.00
420	72	12.97	14.99	0.02
440	28.76	13.8	57.44	19.50

These tests show that the determinated kerosene can be thermally stressed up to 400 °C without any significant change in its composition. The value of olefinic compounds formed at this temperature lies in the internationally accepted limit, 5% of olefins is allowed to be contained in the jet-A kerosene[20]. On the other hand, the undesired carbonaceous solid could firstly be observed at 420 °C.

g.c -m.s analysis:

g.c -m.s analysis of the thermally unstressed kerosene was carried out. C_{11}, C_{10}, C_{12} and C_9 were found as main compounds in the RASCO kerosene respectively. None of olefinic compounds could be indicated in the base kerosene. At 380 °C, small amounts of light olefins were observed (*e.g.* ethylene and propylens). Increasing the temperature to 400 °C leads to a build up of olefins with higher molecular weights. The main compounds formed were methyl 1-butene, trans-2-pentene, 2-methyl-2-buttene, 2-methyl-1-pentene, 2-methyl-2-pentene, 4,4-dimethyl-1-pentene and methyl hexene. Bifunctional olefins or olefins with higher molecular weight were not observed. The appearance of oxygenated compounds like carboxylic acids, alcohols or ketones were not observable. It seems that these compounds are not stable enough for long periods of time (3h) at high temperatures. The g.c and g.c-m.s analysis implied that the C_{11} aliphatic fraction is the main cracking feed. By starting of formation of olefins at 380 °C, the C_{11} content decreases from 20 vol% to 17.1 vol%. The C_{12}, C_{10}, and C_9 values remained unchanged. At 420 °C the cracking process was observed in C_{12}, C_{11}, C_{10}, and C_9. Table 4 illustrates the vol% of these four fractions at different treatment temperatures. It seems from the g.c-m.s analysis that the C_{11} fraction negatively affects the thermal stability of kerosene.

Table 4: Comparison of the vol% of the main aliphatic compounds in kerosene at different temperatures

T/°C	C_9 (vol%)	C_{10} (vol%)	C_{11} (vol%)	C_{12} (vol%)
150-204	1.6	9.5	20	3.80
360	1.6	10	18.2	4.40
380	1.84	10.4	17.1	3.88
400	1.6	9.7	16.1	3.60
420	1.64	6.66	9.97	2.15

CONCLUSION

The n.m.r. spectroscopy and g.c-m.s analysis showed that the Jet fuel produced by Ras Lanuf is

thermally stable up to 400 °C. The thermal degradation starts at 380 °C which leads to trace amounts of olefinic compounds. The g.c analysis indicated that the formation of new olefinic and aromatic compounds is mainly at the expense of the C_{11} aliphatic fraction. The production of carbonaceous deposits was firstly observed at 420 °C.

REFERENCES

[1] R. N. Hazlett 1980. *In Frontiers of Free Radical Chemistry*, W. A. Prior (cd), New York Academic press, 195 p.

[2] R. N. Hazlett, 1991. Thermal oxidation stability of aviation turbine fuels. Philadelphia, US : ASTM, 1991.

[3] CRC literature survey on the thermal oxidation stability of jet fuel 9791, CRC report no 509. Georgia, US: Coordinating Research Council.

[4] S. P. Heneghan, S. L. Locklear, D. E. Geiger, S. D. Anderson and W. D. Schulz, 1993 AIAA *J. Propulsion Power* **9**, 5.

[5] F. R. Mayo andB. Y. Lan 1986 *Ind. Eng. Chem. Prod. Res. Dov.* **25**, 333.

[6] K. T. Reddy, N. P. Cermansky, R. S. Cohen 1989. *J. Propulsion Power* 516.

[7] S. P. Heneghan, W. E. Harrison 1992. Paoer Np. PETR 404.

[8] S. W. Benson and P. S. Nangia 1972. *Accts. Chem. Res.* **12**.223.

[9] C. Song *et.al.*, 1992. *Am. Chem. Soc. Div. Pet. Chem. Prepr.* **37** (2),450.

[10] L. G. Galya and L. R. Rudnick, 1988. *Am. Chem. Soc. Div. Pet. Chem. Prep.* **33**,382.

[11] E. Hirsh and K. H. Altgelt, 1970. *Anal. Chem.* **42**,1330.

[12] D. R. Clutter, L. Petrakis, R. L. Stenger and R. K. Jenson, 1992. *Anal. Chem.* **44**,1395.

[13] J. M. Dreppe, C. Moreaux and H. Castex, 1978. *Fuel* **57**, 435.

[14] S. Gillet, P. Rubini, J. Delpeuch, J. C. Escalier and P. Valentin, 1981. *Fuel*, **60**,221.

[15] S. Yokoyama, D. M. Bodily and W. H. Wiser, 1979. *Fuel*, **58**,162.

[16] D. Brodzki, A. Abou-Akar, G. Djoga-Mariadassan, R. Kandiyti, 1995. *Fuel*, **74**,407.

[17] W. C. Lai, C. Song, 1995. *Fuel*, **74**,1436.

[18] E. Mark, Jr. Myers, Janis Stollsteimer, Andrew M. Winw, 1975. *Anal. Chem.* **47**,2010.

[19] J. David Cookson, C. L. Rolls, B. E. Smith, 1989. *Fuel*, **68**,788.

[20] Specification DERD 2494, Issue 9, Procurement Exccutive, Ministry of Defence, London 1983, 14 #pp.

[21] J. David Cookson, C. L. Rolls, B. E. Smith, 1989, *Fuel* **68**, 776.

[22] S. Gillet, P. Rubini, J. Delpeuch, J. C. Escalier, P. Valentin, 1981. *Fuel* **60**,221.

Petroleum Res. J. Vol. 10 (1998); P. 45-55, 3 Figs.

Determination of Pollutants from Heavy Fuel Oil (HFO) Combustion in Power Plants

L.H. Ali*, A.A. Ejebali* and M.J. Gurbaj*

تعيين المُلوثات الناتجة من حرقِ زيت الوقود الثقيل في محطات توليد الطاقة الكهربائية

لطيف حميد علي و علي عياد الجبالي و محسن جمعة قرباج

تتراكم مخلفات كربونية غير كاملة الإحتراق في قاع وعلى جدران مداخن محطات توليد الطاقة الكهربائية التي يستعمل فيها زيت الوقود الثقيل مصدراً للطاقة الحرارية. تتطلب هذه التراكمات الكربونية الإزالة الدورية لها وقد وجد أن هذه التراكمات ذات حموضة عالية تصل إلى 32.8% وزناً. كما أنها تحتوي مركبات أروماتية متعددة الحلقات المتكاثفة تصل إلى 707 جزء بالمليون.

عند دراسة حالة معزولة لمدخنة إرتفاعها 60 متراً لإحدى المولدات التي تستهلك 17.7 طناً كحد أعلى من الوقود الثقيل وتنتج 65 مليون واط في الساعة الواحدة فقد أظهرت هذه الدراسة تكوّن ما يلي ضمن غازات الإحتراق التي تطلق إلى الجو بواسطة المدخنة.

115.7±15.4 ملغم/م^3 من غاز ثالث أكسيد الكبريت (معدل ست قياسات ومجمع في 80% محلول مائي للكحول الآيزوبروبيلي) و317.5±91.3 ملغم/م^3 من غاز ثاني أكسيد الكبريت (معدل ثلاث قياسات ومجمع في 0.3% محلول مائي لبيروكسيد الهيدروجين) و88.2±75.2 ملغم/م^3 من غاز أول أوكسيد النيتروجين (معدل ثلاث قياسات ومجمع في محلول مائي يحوي 0.1 عياري من حامض الكبريتيك و0.3% بيروكسيد الهيدروجين).

جمعت الغازات أعلاه في نظام مصمم لهذا الغرض من منطقة محددة في جسم المدخنة وسحبت غازات الإحتراق بسرعة 2 لتر في الدقيقة وكانت كمية الوقود الثقيل المحروقة آنئذ تعادل 10.5م^3 بالساعة وكمية الهواء التي تم ضخها إلى الحارقة تعادل 140 ألف م^3 في الساعة.

جرى تعيين تراكيز المعادن الثقيلة في التراكمات الكربونية وفي الطابوق الناري المُبطن لجدار الحارقة وفي الوقود الثقيل قبل الإحتراق وحصلنا على النتائج المبينة أدناه للمعادن المختارة مقاسة بجزء بالمليون وهي على التوالي: الكروم (2.5±271.7، 15.4±386.9، <0.05)، المنغنيز (51.1±853.6، 39.0±544.9، <0.06)، النيكل (567.1±9278.3، 7.9±69.4، 1.7±3.18)، الزنك (2.0±327، 4.9±182.5، 0.1±0.73)، الفناديوم (1916.5±7956.1، 43.1±189.3، 0.8±1.45)، والحديد % (28.0، 0.92، <0.04).

وقد تم تعيين معادن ثقيلة أخرى هي الكادميوم والنحاس والرصاص وجرى تعيين جميع المعادن المذكورة بواسطة تقنية الإمتصاص الذري. ونظراً لخطورة تواجد المركبات الأروماتية متعددة الحلقة في نواتج الإحتراق فقد جرى إستخلاصها بواسطة المذيب ثنائي كلوريد الميثان من التراكمات الكربونية وتمت دراستها وتقدير تركيزها بواسطة كروماتوغرافيا الغاز الشعرية.

Abstract: *Carbon deposits highly contaminated by acids (32.8 wt. % on H_2SO_4 basis), and poly nuclear aromatics (PNA's; 707 ppm) accumulate and need periodical removal from a power station chimney. Heavy fuel oil (HFO) is used as the main fuel.*

SO_3 (115.7±15.4 mg/m^3), SO_2(317.5±91.3 mg/m^3), and NO (88.2±75.2 mg/m^3), in flue gas were determined. HFO consumption was 10.5 m^3.h^{-1} and air flow rate in the burner was140x10^3 m^3.h^{-1}.

*Petroleum Research Center, P.O. Box 6431, Tripoli, G.S.P.L.A.J.

Heavy metals (ppm) Cr: 271.7±2.5, 386.9±15.4 and <0.05; Mn: 853.6±51.1 544.9±39.0 and <0.06; Ni: 9278.3±567.1, 69.4±7.9 and 3.18±1.7; Zn: 327±2.0, 182.5±4.9 and 0.73±0.1; V: 7956.1±1916.5, 189.3±43.1 and 1.45±0.80; Fe(%): 28, 0.92, and <0.04, in carbon deposits, fire-brick linings and HFO, respectively, were determined by atomic absorption spectroscopy. Other heavy metals, namely Cd, Cu and Pb were also determined. Polynuclear aromatics PNA's in CH_2Cl_2 extracts from carbon deposits were estimated by capillary gas chromatography.

INTRODUCTION

Among several orthopogenical activities, combustion of fuels in stationary plants is a major contributor to pollution by some combustion products such as sulfur oxides (SOx), nitrogen oxides (NOx) and particulate matter[1,2,3]. Of most concern, is the combustion of residual fossil fuels, such as heavy fuel oil (HFO).

Another aspect of increasing worldwide attention related to combustion of HFO is the fate of uncombusted and / or reformed organics released into the environment. It is well established now that the combustion of crude oil residues and heavy distillates results in a wide variety of organic pollutants which enter the environment in the form of gas, liquid and solid wastes[4,5]. Among these pollutants, polynuclear aromatic hydrocarbons (PAH; also called: polycyclic nuclear aromatics PNA), make up a class of concern due to their carcinogenic, teratogenic, mutagenic, and chronic low-level hazardous potential that may affect lower and higher organisms.

Heavy fuel oil is used as the main fuel in the Western Tripoli Power Station. The present paper gives the results of a study carried out on deposits in, and emissions from one of five small chimneys (60 m height) in the power station. There are two more bigger chimneys (120 m height). Accordingly, we carried out investigations covering the following aspects:

- Determination of heavy metal contents in the ash of carbon deposits, parent HFO, and in fire-brick lining of chimney.
- Estimation of SOx and NOx release as a result of HFO combustion.
- Studies on water and organic solvents extracts from carbon deposits in the chimney.
- Estimation of uncombusted hydrocarbon release with attempted elucidation of chemical structures of some of the released compounds.

EXPERIMENTAL

Experimental Procedures:

1- Separation of Uncombusted Organic Matter from Carbon Deposits in the Chimney:

Organics were separated using Soxhlet extraction system with toluene or dichloromethane solvents. 50 g (accurately weighed to four decimals) of dried (105°C for 2 h) carbon deposits (bottom; BCD or wall; WCD) were placed in a clean, dried, accurately weighed porcelain thimble, which was then placed in the Soxhlet extractor. 300 ml of solvent was added in the round bottom flask collector, and extraction was continued until no coloured extracts were observed (~12 h). Extraction was stopped, the thimble dried and the extracts were distilled in a rotary evaporator using a mild vacuum. Extracts were accurately weighed .

2- Estimation of Total Uncombusted Hydrocarbons in Flue Gases

Uncombusted hydrocarbons were separated from combustion gases using cooled solvent traps. Two solvents were used in the separation (one at a time), toluene and dichloromethane.

The trapping assembly consisted of:

- Stainless steel tube (180 cm x 0.4 cm internal diameter) to get the gas sample at least one meter deep in the main flow of stack.
- Solvent (aq. NaOH 1.0 N) traps
- Silica gel trap to protect the vac. pump.
- Vacuum pump equipped with gas flow meter and was adjusted to a flow of 1.5 l. $min.^{-1}$

When everything was set, the stopcock was opened, the pump was turned on, and the gas sample was drawn up to 500 liter total volume. At this point, operation was stopped,the solvent was distilled under mild vac. using a rotary evaporator, and the uncombusted organics were accurately weighed. Refer to Figure-1 for a diagram of the operation.

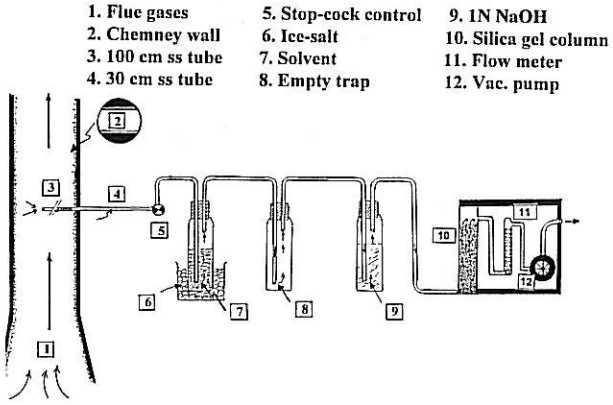


Fig. 1. Flue gas trap for uncombusted organics.

3- *Determination of Total Acidity of Flue Gases:*

A similar trapping system to that used in (2) above was used to determine the total acid content of flue gases. Two traps were used, the first one contained 500 ml, 2 N NaOH aqueous solution and the second one (between the first and the pump) was empty. The flow rate was adjusted to 1.5 l/min. and the operation was stopped after 500 liters were drawn. The amount of trapped acids was determined from the back titration of the NaOH solution. Acids were determined on a H_2SO_4 basis.

4- *Determination of Total Acidity of Water Extracts from Carbon Deposits:*

100 g of carbon deposits (B.C.D and W.C.D, one at a time) were refluxed (1 h) with 500 ml of distilled water. The mixture was then filtered and the deposits were washed several times with distilled water. The filtrate and the washings were combined and the volume was made up to 1 liter in a volumetric flask. The pH of the previous solution was measured. Samples of 50 ml of this solution were titrated against a standard 0.2 N NaOH solution using phenolphthalein as indicator. The total acid content was determined on a H_2SO_4 basis.

5- *Determination of Sulfate Ion in the Aqueous Extracts:*

The method used was that of **ASTM-D516**[6].

6- *Determination of Iron Content in the Aqueous Extracts from Carbon Deposits:*

The method used was that of **ASTM-C114**[7], which is basically used for the analysis of hydraulic cement .

7- *Determination of Ash Contents:*

The methods used were those of **ASTM-D482-(87)**,or **ASTM-D3174-(79)**[8] depending on the sample, whether liquid or solid.

8- *Determination of Heavy Metal Contents in Carbon Deposits:*

The method used with carbon deposits was that of **ASTM-D3683**[9].

9- *Determination of Heavy Metal Contents in Heavy Fuel Oil:*

A suitable weight of sample (10 g) was ashed into a platinum dish at 500°C in a muffle furnace with 0.5 g of p-toluenesulfonic acid. When ashing was completed (~30 min.), the residue was warmed gently with 10 ml of nitric acid (25%), stirring and crushing the ash with a glass or PTFE rod. The slurry was transferred to a 50 ml calibrated flask, washed with a further 10 ml of nitric acid (25 %) and 5 ml of cesium chloride solution (1 %) and diluted to the mark.

Calibration solutions were prepared from a stock standard and they contained the same concentrations of nitric acid and cesium chloride as the sample solutions.

10- *Separation and Determination of Individual Polluting Gases: SO3 SO2 and NO.*[1]

(a) Collection and Determination of SO_3:

200 liters of flue gases, withdrawn from the chimney at a rate of 4 l. min^{-1}. were passed through a liquid trap of 80% iso propyl alcohol in distilled water (400 ml IPA + 100 ml H_2O). The gases were kept warm by wrapping the stainless steel connecting tube with asbestos tape, since SO_3 dew point is about 44°C. At the end of the experiment, SO_3 content in the trap was determined by titration against 0.01 N NaOH aqueous solution using phenolphthalein as an indication.

(b) Collection and Determination of Total SO_2+NO

Gases leaving the SO_3 trap in (a) above, were split by a three-way stop cock and were passed simultaneously at a rate of about 2 l. min^{-1}. into two liquid traps; one for total SO_2 + NO and the other for NO alone.

The total SO_2 +NO stream was allowed to pass through 500 ml of 0.3 % H_2O_2 aqueous solution. At the end of experiment, SO_2 + NO content (after being oxidized to SO_3 + NO_2 by H_2O_2) was determined by titration against 0.01 N NaOH aqueous solution using phenolphthalein as an indicator. The SO_2 content in flue gas was deduced by subtracting the corresponding value related to NO which is determined in (c) below.

(c) Collection and Determination of NO:

The split stream of stack gases from (b) above was passed through 500 ml of 0.1 N H_2SO_4 in 0.3% H_2O_2 aqueous solution. A diagrammatic representation of the operations is given in Figure-2. At the end of the experiment, the solution was made alkaline with 1 N KOH and was evaporated to dryness; gently without any spattering (about 24 h).

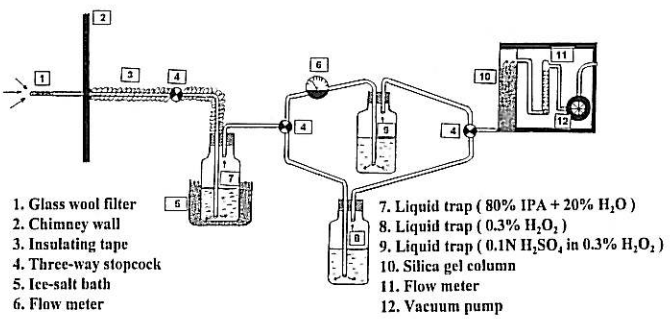


Fig. 2. Liquid trap for SO_3, SO_2 and NO.

10 ml of phenoldisulfonic acid reagent (PDS) "see *d* below" was added to the residue from evaporation, the solution was shaken and was transferred quantitatively, to a 100 ml volumetric flask, using distilled water. Visible light absorption in the range 400-430 nm was obtained (the solution may be diluted if necessary). The concentration of NO_2 was determined from a calibration curve of concentration Vs absorption intensity in the range 400-430 nm of KNO3 standard solutions containing known amounts of PDS reagent in both samples and reference cells.

(d) Preparation of PDS Reagent:

It is prepared as follows:

Phenol	25 g
Conc. H2SO4	150 ml
15% Oleum	75 ml

11- Gas Chromatographic Experimental Conditions for the Determination of Poly-Nuclear Aromatics (PNA):

The chromatographic conditions employed by us in the separation of PNA's are listed in (A) below. Meanwhile, the GC-Conditions employed by the American Environmental Protection Agency [EPA] for the separation of the 16 standard PNA's[125], are listed in (B). The variation in conditions, as given in the two sets (A and B), may afford an explanation for the small differences in the retention times of some of the expected PNA's compared with the standard ones.

Chemicals and Instruments:

- Chemicals used were of analytical grade obtained from Aldrich, UK.
- GC carried out using PACKARD 439.
- Heavy metal determined using AAS/A. A-1475,
- Sulfur determined using ANALIR, Analyzer instrument.
- GC 312 pumps used to withdraw gases from chimney
- pH meter used was KNICK DIGITAL-pH-METER 646

A	B
PRC- GC- Col . Conditions	**EPA - 610 / GC- Col. Conditions**
Column: 25m x 0.25mm (L x ID) WCOT CP-Sil CB (df = 0.12μm)	Column: 25m x 0.25mm (L x ID) Ultimetal WCOT CP-Sil PAH CB (df = 0.12μm)
Temperature: 35°C - 280°C rate 5°C/ min.$^{-1}$	Temperature: 70 C - 300 C / min-1.
Carrier gas: N_2, 60 KPa (0.6 bar,); 25ml/min^{-1}.	Carrier gas: H2, 100 KPa (1.0 bar, 15 psi); 30 cm/s
Injector: spliter, 100 ml / min^{-1}. (T = 300°C)	Injector: spliter, 100 ml / min-1. (T= 325°C)
Detector: FID, 1 x 10 -11AFS (T = 300°C)	Detector: FID, 2^3 (T= 350°C)
Sample size: 1.0μl	Sample size: 0.5μl

- Muffle furnace LINN. HIGH THERM VMK22 used for ashing.

RESULTS AND DISCUSSION

The *Western Tripoli Power Station*, first established in 1976, is situated on the Mediterranean shore, about 20 km west of Tripoli center. Heavy fuel oil (HFO) is used as the energy source for steam generation. The station is composed of two power plants, the descriptions of each are given in Table 1.

There also exists a desalination plant and treatment units. The power station is surrounded by farms and village residential communities from all directions except the north side. Prevailing wind is from north to south in most seasons, thus, farms and populations are exposed to pollution from emissions from this power station.

Figure -3 gives an illustrating diagram for the boiler, gas flow, sampling location and definition of carbon deposits (bottom carbon deposits, B.C.D and wall carbon deposits W.C.D with respect to chimney).

Table 1. Western Tripoli Power Station.

Property	Plant A	Plant B
- No. of generators	5	2
- Capacity; mega watt.h^{-1}	5x65	2x120
- Stack height; meters	60	120
- Amount of HFO consumed, Tons.h-1 at max. loading	17.7	28.5

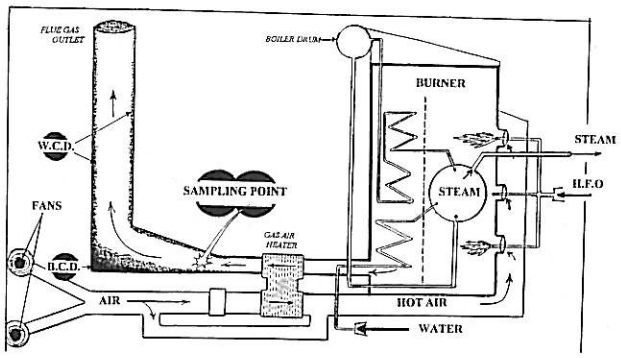


Fig. 3. Boiler air and gas flow.

Temperatures in the burner and boiler zones are also indicated.

Sampling and operation conditions with other information of interest are given in Table-2. It is obvious that our results and conclusions represent only a small portion of operations taking place at the power station. All our investigations were carried out on one of the five small chimneys in plant A (Table-1), defined as Unit 2.

In our investigations, we focused first on the carbon deposits (C D) in the chimney. A pile of over 50 cm deep of these deposits was noticed on the chimney's floor (B.C.D), and about 15 cm thick deposits on the inside walls (W.C.D). It is well established that incomplete combustion of fossil fuels produces carbon deposits, along with a variety of reformed and/or partially oxidized hydrocarbons. It is also expected that carbon deposits will be contaminated with inorganic acids as a result of the production of acid gases during combustion.

Extraction of CD with CH_2Cl_2 in a soxhlet system produced a higher hydrocarbon content, but less combustibles in WCD (Table-3). The results in this table further indicate a very high iron content in the ash of CD (especially in BCD). This prompted us to carry out full analysis on heavy metals content in BCD, WCD the fire brick lining of the chimney's interior, and ash in the parent HFO. The results are given in Table-4. Fire brick (FB) is also used to line the interior of the burner. The results in Table-4 indicate that FB may be the source of the relatively high contents of Fe, Mn, Pb, Cr, Zn, and Cu in the carbon deposits. On the other hand, the HFO is a considerable precursor of Ni and V.

The water extracts from carbon deposits was found to be highly acidic. This is to be expected given the type of fuel used (HFO) and the combustion conditions. The results on pH and amount of acid in CD on the basis of H_2SO_4 equivalence, are given in Table-5 .

Table 2. Sampling and operation condition*

Sampling conditions			Operation conditions			
Sample No.	Sample type	Sampling date	Air flow (m3h)	Fuel (ton/h)	Power (mega watt)	Stack temp. (°C)
1	Hc.	19.1.95	170	13	40	135
2	Hc.	19.1.95	170	13	40	140
3	T.acid	26.1.95	160	15.5	42	140
4	T.acid	26.1.95	145	12.5	40	135
5	Hc.	30.1.95	160	13	42	135
6	Hc.	30.1.95	160	13	42	135

* As designed.
- Sampling location : Unit 2.
- Sampling duration : 4 h.
- Flow rate (l.min^{-1}): 2
- Sample vol. (l): 500.
- Combustion temp. C°: 1370.
- Hc: hydrocarbons.
- T. acid: Total acids.

Table 3. Bottom & wall carbon deposits analysis

Sample	% Ash	% Iron	% Organics (% hydrocarbons)	% Combustables (and/or decomposebles)
B C D	47.67	28	0.11	52.33
W C D	66.5	4.6	0.43	33.5

Table 4. Average concentration(X) of heavy metals(1)

Element	B C D (ppm)	W C D (ppm)	F B (ppm)	H F O (ppm)
Cd	59.54±4.3	27.7±3.1	7.1±0.46	< 0.06
Cr	271.7±2.5	49.7±2.8	386.9±15.4	< 0.05
Cu	173.9±11.3	47.2±2.1	38.0±2.9	< 0.04
Fe %	28.0(2)	4.6(2)	0.9(2)	< 0.04
Pb	4161.2±11.5	259.5±10.4	51.7±1.5	< 0.34±0.6
Mn	853.6±51.1	1828.9±70.8	544.9±39.0	< 0.06
Ni	9278.3±567.1	92.3±18.4	69.4±7.9	3.18±1.7
Zn	327±2.0	74.7±6.1	182.5±4.5	0.73±0.1
V	7956.1±1916.5	1825.8±147.2	189.3±43.1	1.45±0.8

(1) Average of three determinations.
(2) By gravimetric & Titrimetric Analysis.A single determination was conducted

Table 5. Acids in bottom & wall carbon deposits

Sample	PH	N* (g.ml^{-1})	Total acid (H_2SO_4 basis) (g/l)	% Acid in deposits (H_2SO_4 basis)	SO_4=** (ppm)
B C D	1.5	0.015	16.4	32.8	11145
W C D	1.6	0.008	9.8	19.6	5390

* N Grams of NaOH needed for neutralization of acids
** Determined gravimetrically

It is well established that sulfur in fossil fuels converts mainly to SO_2 on combustion of fuel[2,3].

$$\underset{\text{fossil fuel}}{C, H, S, ...} + O_2 \longrightarrow \underset{99\text{-}98\%}{SO_2} + \underset{1\text{-}2\%}{SO_3} + CO_2 + H_2O + \text{etc.} \quad (1)$$

It is also well documented in literature, that active conversion of SO_2 to SO_3 is catalyzed by Fe and Mn oxides present in the fly ash of the same heavy fuel employed[3].

$$SO_2 + {}^1/_2O2 \xrightarrow{Fe/Mn} SO_3 \quad (2)$$

$$SO_3 + H_2O \longrightarrow H_2SO_4 \quad (3)$$

Fe and Mn salts are also present in the composition of fire bricks lining the interior of the burner and chimney (refer to Table-4) and may play an important role in this conversion (Equation-2) through surface catalysis. This may

also account for continuous abrasion of the lining and accumulation with the carbon deposits. To further supplement and justify the choice of H_2SO_4 equivalence for the estimation of total acid content in CD, a gravimetric determination of sulfate ion content in the aqueous extracts from CD was performed. The results are given in Table-5. BCD contained more than twice the amount of sulfate ions than WCD.

Separation of the principle polluting gases: SO_3, SO_2 and NO individually from flue gas, using liquid traps as shown in Figure-2, made reliable assessment of the contribution of each gas possible. The choice of the specified liquid traps is based on previous work[1]. Thus, the determination of SO_3 in flue gas is based on the work of Alyea and Backstrom[10] who found that several higher alcohols inhibited the oxidation of dissolved SO_2. Flint[11] selected isopropanol (IPA) because it is miscible with water, its inhibiting action extended over long periods of time, and the solubility of SO_2 in IPA solutions was considerably lower than in distilled water. Absorption in 80 % IPA has been the most widely used collection method[11,12] for SO^3 in power plants.

Aqueous hydrogen peroxide absorbing solution has been widely used for the collection of SO_2[11,13], where:

$$SO_2(g) + H_2O \longrightarrow H_2SO_3\ (aq.) \xrightarrow{H_2O_2} H_2SO_4\ (aq.) \quad (4)$$

Collection of SO_2 in H_2O_2 is the technique required by EPA for checking compliance with new source performance standards (power plants etc.) under the Clean Air Act of 1970[15].

Nitric oxide (NO) is the only oxide of nitrogen present in significant concentrations at flue gas temperatures. It is mainly formed as a result of the reaction of O_2 and N_2 of the air at flue combustion temperatures. Thermodynamically, the oxide is unstable and dissociates back to its elements at all temperatures:

$$^1/_2\ N_2 + {}^1/_2\ O_2 \rightleftharpoons NO \quad (5)$$

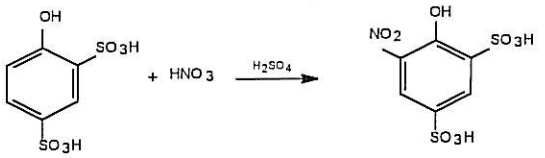
Phenoldisulfonic acid (PDS) is the most widely used reagent for NO_x determination in flue gases and it has been adopted as a standard method by EPA[13,14] and other standards[16]. Beatty, *et. al.*[17] used 0.1N H_2SO_4 in 0.1% H_2O_2 as the absorbing solution and recently up to 0.4% H_2O_2 has been used. The peroxide serves a two-fold purpose, namely to oxidize any nitrate and to convert sulfite, an interference, to sulfate i.e.:

$$NO + H_2O_2 \longrightarrow NO_2 + H_2O \longrightarrow HNO_3 \quad (6)$$

$$SO_2 + H_2O_2 \longrightarrow SO_3 + H_2O \longrightarrow H_2SO_4 \quad (7)$$

H_2SO_4 does not interfere with the quantitative color production which will be explained below.

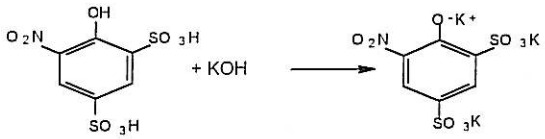
After absorption, the solution is made alkaline with potassium or sodium hydroxide and slowly evaporated to dryness to avoid spattering losses. PDS is then added to the dry solid residue and a nitration reaction takes place:



(8)

Phenol-2,4-disulfonic acid (PDS) | Phenol-6-nitro-2,4-disulfonic acid (PNDS) | (Formed in solution)

The yellow colour produced on making the solution alkaline is due to the ionization of the phenolic proton from the 6-nitrophenol-2,4-disulfonate:



(9)

PNDS | Yellow

The yellow color produced is measured between 400 and 430 nm with a spectrophotometer. The color intensity is related to concentration and assessed quantitatively from a calibration curve.

The results obtained for determining SO_3, SO_2 and NO concentration in milligrams per cubic meter (mg/m3) of flue gas, are given in Table-6 (a and b). It is obvious from these results that considerable conversion of SO_2 to SO_3 does take place under the combustion conditions. It is well established that only 1 to 2 percent of SO_3 is

usually produced on burning in air of sulfur containing fossil fuels such as HFO. The average results on SO_3 content in Run No.'s 1,2 and 6 in Table - 6a, and those in Run No.'s 1,2 and 5 in Table - 6b, on SO_2 content, indicate that SO_3 concentration (in mg/m^3) is about 28% that of the total SO_x produced during the combustion of HFO containing 0.5% sulfur. This strongly points that a considerable catalysis is taking place. Such catalytic effect is probably occurring through the action of Fe and Mn oxides in the ash and/or through the action of other metals present in the composition of the fire-brick lining in the burner and chimney walls.

Table 6a. Concentration of SO3[1] in flue gas from the combustion of HFO[2][3] in Western Tripoli Power Station

Run No.	Vol. of 0.01N NaOH needed (ml)	Total NaOH consumed (g/m^3)	H_2SO_4 equivalence (mg/m^3)	SO_3 equivalence (mg/m^3)	Date of run
1	2.6	0.130	159.3	130.1	30.1.96
2	2.3	0.115	140.9	114.6	30.1.96
3	2.0	0.100	122.5	100.0	6.2.96
4	2.6	0.130	159.3	130.1	6.2.96
5	1.9	0.095	116.4	94.6	6.2.96
6	2.5	0.125	153.1	124.5	6.2.96

(1): Collected in 80%IPA aqueous solution .
(2): HFO consumption 10.5 $m3.h^{-1}$ and air flow rate in the burner $140x10^3$ $m^3.h^{-1}$
(3): HFO sulfur content is 0.5% .
- Sample collection flow rate 2 $l.min^{-1}$, vol. of gas collected = 200L
- Liquid trap volume = 500 ml.
- Titrated portion volume = 20 ml.

Noticeable concentration of NO is also produced as a result of the operating conditions in this power plant. An average value of 88.2 mg/m^3 NO is produced in the Run No.'s 1,2 and 5 (Table - 6b) compared to 317.5±91.3 mg/m^3 (Table 6b) and 115.7±15.4 mg/m^3 (Table 6a), for SO_2 and SO_3 respectively. This comparison further indicates that about 17% of the total (SO_x + NO_x) emission is in the form of nitrogen oxide (NO) expressed in mg/m^3. Chemical conversions in the manner outlined earlier (equations 1, 2, 3 and 5) might take place producing the observed SO_x and NO_x distribution.

We thought it is necessary to put some emphasis on uncombusted and/or reformed organics released into the environment during the combustion of fossil fuels. By far, the main anthropogenic source of PNA's is incomplete combustion of fossil fuels.

Up to date, the power of the combined capillary column GC/MS system is the top analytical technique for the separation, estimation and identification of individual PNA's[18-23]. In our laboratory, we tried to throw some light on PNA's in CD using capillary column GC only.

In a recent publication[24], emphasis on dichloromethane (CH_2C_{12}) as a model PNA solvent was registered, therefore, we used CH_2Cl_2 to extract (soxhelt), and to trap organics from CD and flue gases respectively. The results on total amount of organics trapped were 998 ppm, 4280

Table 6b. Concentration of SO_2[1] and NO[2] in flue gas from the combustion of HFO[3] in Western Tripoli Power Station

Run No.	Vol. of 0.01N NaOH needed (ml)	Total NaOH consumed (g/m^3)	Portion of NaOH reacting with HNO_3 (mg/m^3)	Portion of NaOH reacting with H_2SO_4 (mg/m^3)	SO_2 equivalence (mg/m^3)	NO equivalence (mg/m^3)	Date of run
1	3.6	0.36	69.1	290.9	231.6	51.8	30.1.96
2	6.2	0.62	233.1	386.9	307.6	174.8	30.1.96
3	3.2	0.32	-	-	-	-	6.2.96
4	3.8	0.38	-	-	-	-	6.2.96
5	5.7	0.57	50.6	519.4	413.4	38.0	6.2.96

(1): Collected in 0.3% H_2O_2 aqueous solution, then determined by titration againest NaOH.
(2): Collected in 0.1N H_2SO_4 in 0.3% H_2O_2 aqueous solution, then determined spectrophotometriclly using PDS method .
(3): HFO consumption 10.5 $m^3.h^{-1}$ and air flow rate in the burner $140x10^3$ $m^3.h^{-1}$.
- Sample collection flow rate 2 $l.min^{-1}$, vol. of gas collected = 100L
- Liquid trap volume = 500 ml.
- Titrated portion volume = 20 ml.

ppm and 0.0848 g/m^3 for BCD, WCD and flue gases respectively.

In order to throw light on the nature of the CH_2Cl_2 extracted organics from CD, detailed capillary column gas chromatographic investigation was carried out on three extracted samples from each of BCD and WCD. The specification of the GC column, the running conditions and results are given in Table-7 for BCD and in Table-8 for WCD. Although running conditions are not exactly matched with those given in literature[25] on the conventional sixteen PNA's proposed by the American Environmental Protection Agency [Project EPA - 610], tentative comparisons of our results and relevant observations and conclusions may be drawn. A major conclusion is that several PNA's are present in the CH_2Cl_2 extracts from

Table - 7 GC of CH_2Cl_2 extract from bottom carbon deposits (B C D)

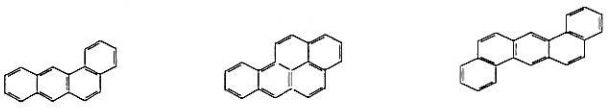
B C D_1		B C D_2		B C D_3		EPA[25]	
R.T.O (min)	CONC. (ppm)	R.T.O (min)	CONC. (ppm)	R.T.O (min)	CONC. (ppm)	Name formula	R.T.S (min)
-	-	-	-	-	-	Naphthalene $C_{10}H_8$	4.24
10.5	40.6	10.2	11.1			Acenaphthylene $C_{12}H_8$	10.65
-	-	-	-	11.4	11.00	Acenaphthene $C_{12}H_{10}$	11.8
-	-	-	-	-	-	Fluorene $C_{13}H_{10}$	15.16
-	-	-	-	-	-	Phenanthrene $C_{14}H_{10}$	21.28
23.8	44.00	-	-	-	-	Anthracene $C_{14}H_{10}$	21.64
-	-	-	-	-	-	Fluoranthene $C_{16}H_{10}$	29.94
-	-	-	-	-	-	Pyrene $C_{16}H_{10}$	31.36
40.4	364.7	40.1	402.8	39.9	322.0	Benz[a]anthracene $C_{18}H_{12}$	40.51
40.7	32.0	40.4	37.5	42.5	31.5	Chrysene $C_{18}H_{12}$	40.80
47.8	5.7	47.5	61.5	46.9	26.00	Benzo[b]fluoranthene $C_{20}H_{12}$	48.08
49.3	29.1	48.6	18.4	-	-	Benzo[k]fluoranthene $C_{20}H_{12}$	48.31
51.0	64.00	49.00	75.9	51.7	15.5	Benzo[a]pyrene $C_{20}H_{12}$	49.85
56.0	28.2	55.6	20.3	55.3	28.7	Benzo[ghi]perylene $C_{22}H_{12}$	56.72
-	-	57.6	157.0	57.6	101.0	Indeno[1,2,3-cd]pyrene $C_{22}H_{12}$	57.38
58.0	8.6	58.1	18.3	-	-	Dibenz[ah]anthracene $C_{22}H_{14}$	58.00
Total GC detected PNA (ppm)	616.7		968.4		535.7		
Total Hc content (ppm)	906		1183		906		

R.T.O = Retention time / observed.
R.T.S = Retention time / standard.

BCD and WCD, but we cannot assign accurately any specific retention time to a certain PNA member. An observation worth mentioning from Tables 3, 7 and 8 revealed the amount of organics in WCD is about four folds higher than that in BCD. This suggests that the higher we go up in the chimney the higher the concentration of expected PNA's. In other words, a noticeable release of PNA's occurs as a result of burning HFO as a source of energy at the *Western Tripoli Power Station.*

In Table 9 (a and b), the structures of some strong carcinogenic PNA's and the percent of total area measured by GC of related carbon numbers, are listed.

Table 10
(a) Structure of some carcinogenic PNA's



Benzo[a]anthracene ($C_{18}H_{12}$) Benzo[a]pyrene ($C_{20}H_{12}$) Di-Benzo[ah]anthracene ($C_{22}H_{14}$)

(b) Percent of total area measured by GC

Cx	BCD_1	BCD_2	BCD_3	average BCD	WCD_1	WCD_2	average WCD
C_{18}	44	48.6			13.7	17.3	15.5
(40.51)	(40.4)	(40.1)	(39.9)		(40.1)	(41.5)	
C_{20}	10.7	13.2	4.6	9.3	3.0	3.9	3.5
(49.85)	(51.0)	(49.0)	(51.7)		(50.8)	(46.9)	
C_{22}	10.3	16.6	14.3	13.7	2.4	5.1	3.8
(58.0)	(58.0)	(58.1)	(57.6)		(56.9)	(56.9)	

*Values in brackets represent retention times in mints.

CONCLUSIONS AND RECOMMENDATIONS

In a very broad sense, two major conclusions may be drawn from this study:

1- Flue gases form the combustion of heavy fuel oil (HFO) in *Western Tripoli Power Station* and the amount of fuel combusted daily may pose health hazards to people, animals, and plants and cause property damage under certain meteorological conditions; when air is stagnant. However, in order to give fair assessment of the effects of pollutants; SOx, NOx, Particulate, PNA's etc. it is imperative to conduct seasonal monitoring at specified distances from the station in all directions (except North), taking meteorological conditions into consideration.

2- Highly acidic, extremely enriched heavy metals and PNA's containing carbon deposits, which are removed periodically from the chimneys, pose serious dangers no matter where these deposits are disposed of; on land or in the sea. We recommend the following scheme to deal with these deposits.

i- Adjusting the combustion operation conditions, or injecting steam to reduce the carbon deposits formation to minimum.

ii- When the above is not attainable, the deposits may be washed with a dilute base (*e.g.* 0.01 N NaOH) to neutralize the acidity.
The acid free deposits may be used as a solid fuel, after mixing with a petroleum pitch, or be used as a filler in road paving.

AKNOWLEDGEMENTS

We, the authors of this work, wish to convey gratitude to the management of the Petroleum Research Centre for permission to publish this work. We also wish to aknowledge thanks to the management of the Western Tripoli Power Station (WTPS) for their understanding and unlimited cooperation. Special thanks are due to the chief engineer at WTPS, Mr. Muhsen Shiglabo for his sincere help during the course of conducting the field experiments.

REFERENCES

[1] Driscoll, J. N. 1974 flue Gas Monitoring Techniques *Ann Arbor Science* (1-9) .

[2] Stoker, S. H. and Spencer S. I. 1976. *Environmental Chemistry; Airand Water Pollution* Scott, Foresman and Company, Brighton, England.

[3] Ali, L. H . 1987, *Industrial Pollution: Sources, Chemistry and Control* – University of Mosul Publication Registration No. 1241 1987. The National liberary , Baghdad, Iraq (in Arabic).

[4] Sadeghi, M.A., Sharma, M.M.,and Yen, T.F. 1982, *Proceedings, 17th Intersociety Energy Conversion Engineering Conference*, **2**, 899.

[5] Yen, T.F. 1984, *Proceedings, Specialty Conference on Environmental Engineering* 460 P.

[6] ASTM - 516 - 68 Re- a pproved 1974 Determination of sulfate ion in water.

[7] ASTM-C114-77 1977 Chemical analysis of hydraulic cement.

[8] (a) ASTM-D482-87 1987 Ash from petroleum products.

(b) ASTM-D3174-73 Re-approved1979 Ash in the analysis of coal and coke.

[9] ASTM-D3683-78 Re-approved1989. Trace elements in coal and coke by atomic absorption.

[10] Alya, H.N. and Backstrom, H.L., 1929 *J. Am. Chem. Soc.*, **51**, 108.

[11] Flint, D. 1948 . *J. Soc. Chem. Ind.* **67**, 2.

[12] Gartrell, F.E., *et.al.* 1963. *Am. Ind. Hyg. Assoc. J.*, **24**, 13.

[13] Corbett, P.F. 1948, *J.Soc. Chem. Ind.*, **67**, 227.

[14] Seidman, E.B., 1958. *Anal. chem.*, **30**,1680 .

[15] EPA Standards, 1971 Standard of Performance for New Stationary Sources Federal Register, 36 No.247, P 24876, Method 7.

[16] ASTM D1608-60, 1971., *ASTM Book of Standards*, Part 23.

[17] Beatty *et.al.*, 1943 Determination of nitrogen by the PDS method. *Bureau of Mines*, R13687.

[18] Grimmer, G., Bhonke, H., and Fresenius, A. 1972. *Anal. Chem.* **45**, 261.

[19] Lao, R.C., Thomas, R.S., Oja, H., and Dubbios, L. 1972, *Anal. Chem.* **45**, 310.

[20] Lao,R.C., Thomas, R.S., and Monkman, J.L. 1975, *J. Chromatogr.*, **112**, 618.

[21] Hites, R.A., and Biemann, W.G. 1975. *Adv. Chem. Ser.*, **147**,188.

[22] Hase, A., and Hites, R.A. 1976. *Geochem. Cosmochim. Acta.*, **40**, 1141.

[23] Bieri, R.H., Cueman, M.K., Smith, C.L., and Su., C.W. 1978. *Int.J.Environ. Anal. Chem.*, **5**, 293.

[24] Sadeghi, K.M., do Nascimento, H.C.G., Sadeghi, M.A., Wang, L.S., Wang, Y., and Yen, T.F. 1994. *Fuel Sci. Tech. Intern.*, **12**, 1393.

[25] (a) *Janssen Chemical Acta.* (1992), **10**, No. 3.
(b) *Chrompack Catalogs of Chemical Separation.*

Petroleum Res. J. Vol. 10 (1998); P. 57-59, 2 Figs.

The Bahi Formation – Its stratigraphic position, western Sirt Basin, Libya

Milad Ali Ghummed*

تكوين الباهي – وضعه الطباقي (الإستراتجرافي) بمنطقة غرب حوض سرت، ليبيا

ميلاد علي غميض

يعتقد أغلب الجيولوجيين أن العمر النسبي لصخور تكوين الباهي في منطقة غرب حوض سرت ينتمي إلى ما قبل عصر الماستريخشان غير أن هذه الدراسة تشير إلى إحتمال أن يكون عمر الجزء العلوي من هذه الصخور في بعض أجزاء المنطقة أكثر حداثة من ذلك وربما يصل إلى عصر الدينيان. وتوصي هذه الدراسة بمزيد من التمحيص بالنسبة لعمر هذا التكوين ووضعه الطباقي (الإستراتجرافي) نظراً لأهميته كصخر حامل للنفط في بعض الحقول. ولتحقيق هذا الهدف ربما يمكن إستخدام الطفل المحتوى والبالينومورفات وكذلك العناصر المشعة بمعدن الجلوكونايت الموجود بالتكوين.

The subsurface marine succession in the western Sirt Basin (Fig. 1) is normally underlain, in many places, by a sandstone unit known as the Bahi Formation. Lithologically, it commonly consists of sandstone and pebbly sandstone with a clay matrix and interbeds of siltstones, conglomerates and shale and its thickness varies from zero to a maximum of over 400 feet (Barr and Weegar, 1972).

The Bahi Formation unconformably overlies various lower Palaeozoic rocks, mostly Cambro-Ordovician Hofra Formation (Orthoquartzites) and is overlain by marine sediments with a sharp and conformable to gradational contact (Fig. 2).

The generally mottled nature of the siltstones and shale and the red staining of the sand grains may indicate a continental origin. The presence of glauconite in the uppermost 10-20 feet could be considered as a sign of marine origin.

The thickness variation is believed to have had been caused principally by the palaeotopography. The provenance, being mostly continental, the time span of its subaerial exposure, therefore, is expected to have had also played a very significant role in this variation. This role can obviously be explained by the act of weathering and erosion processes on the highs accompanied by the settling of the yielded product in the lows.

The age of Bahi Formation in western Sirt Basin seems to have had been suggested during the early stages of exploration for oil and had never been changed in the work that followed. It was considered older than Maastrichtian (Barr, 1972, Barr and Weegar, 1972 and Sughair, 1992). This inferred age decision had, most likely, been based on the assumption that the total inundation of Sirt Basin took place during the Maastrichtian Stage and, consequently, marine carbonate deposits were assumed to have had been laid down all over the basin during this stage. In this case, the provenance and the site of deposition of this formation, which are mainly continental, were

*Petroleum Research Centre, P.O. Box 6431, Tripoli, G.S.P.L.A.J.

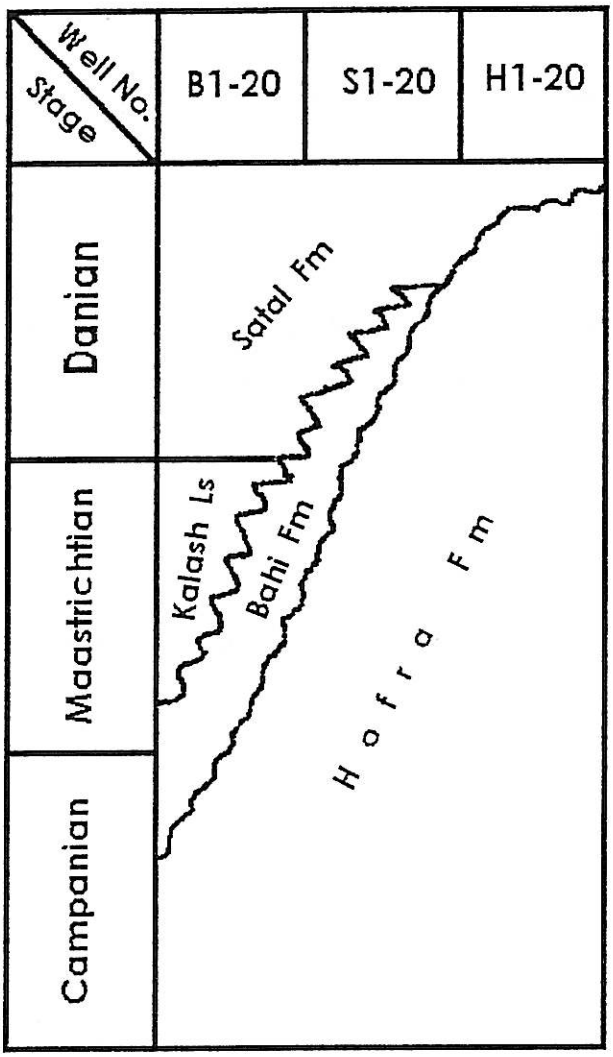


Fig. 1. A map showing the geographical distribution of the Danian Islands (eminences).

both considered non-existent after the Campanian Stage or early Maastrichtian time.

The age aspect of this formation, however, does not seem to have received enough attention from geologists. Its virtual barrenness of fossils had possibly contributed to the difficulties faced in its age determination and, therefore, it was decided stratigraphically.

The idea of throwing some light on this aspect occurred to the author during a regional investigation of the Palaeocene succession in the area (Ghummed, 1997). The interest in this problem arose from finding out that the minimum thickness of the Danian marine strata (limestone overlain by shale) is occurring in H1-20 well, where it is found in direct contact with the Hofra Orthoquartzites. This minimum thickness, measuring less than 120 feet, is considered less likely to represent the full Danian time by all measures. Therefore, a considerable time-proportion of the Danian Stage is considered to be represented by non-deposition and, most likely, erosion at this location. This proportion could be as high as four fifths of the stage as can be figured out knowing that the thickness of the Danian marine strata, where fully developed, is normally about 1000 feet, especially in the relatively stable areas. This perhaps can be interpreted, in terms of time that Hofra Formation remained, in some parts of the area, subaerially exposed for a considerable period of time during the Danian Stage. This period is unlikely to have had no impact on the exposed rocks with regard to weathering, erosion and deposition.

The present work, however, shows quite clearly that Hofra Formation continued subaerially exposed in many parts of the area, especially in the so-called Azzahrah-Al Hufrah and Al Bayda platforms (Fig. 1), until sometime through the Danian Stage forming some sort of islands (eminences). These islands are considered to be the sole source of the sand found in the area. It is normal, however, to expect that these bold areas to be subjected to weathering and erosion and, eventually, the settling of the product of these processes in their environs. Therefore, it is quite possible to consider part of Bahi Sandstone to be Danian in age.

The sandstone thickness in these islands varies from zero to over 300 feet in places. The Maastrichtian-Danian contact within this formation is rather difficult to place in many cases, whereas in others it is possible to consider the whole sand as belonging to the Danian, e.g. in UU1-11 Well where more than 300 feet of strata consist of interbedded sandstone and chalk (based on stratigraphical correlation). This interbedding is undoubtedly an additional very sound proof of assigning a Danian age to, at least part of, this sandstone because the chalk is most likely Danian deposits.

The onlapping nature of the formation and the certainty of subaerial exposure of its source during Danian allow the suggestion that it does not only straddle stratigraphically the Campanian-

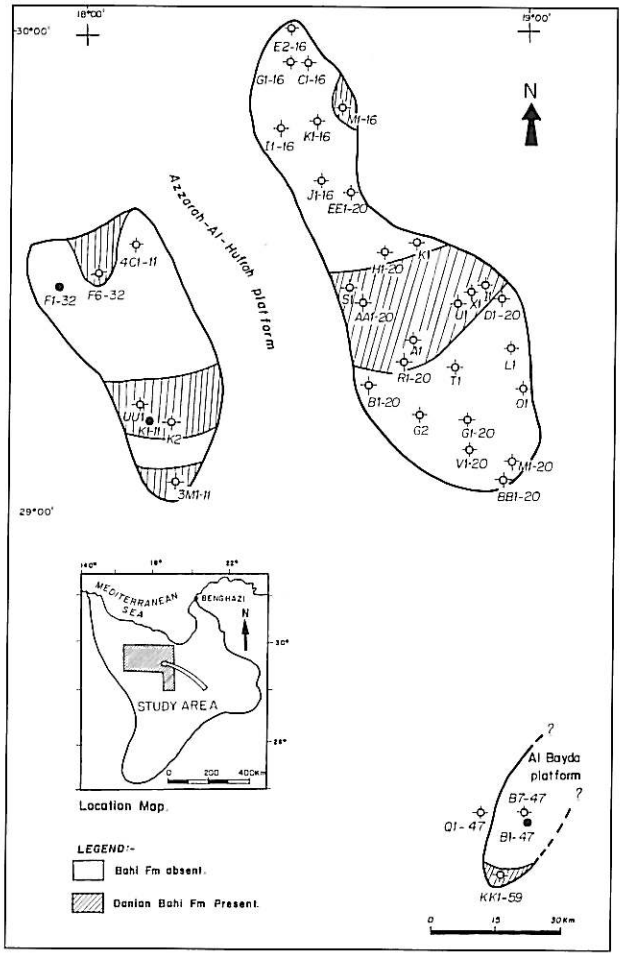


Fig. 2. A sketch diagram showing the inferred occurrence of the Bahi Fm.

Maastrichtian boundary, but also that of the Cretaceous-Tertiary and, therefore, its age can rightly be considered extending into Danian. The re-investigation of the formation with regard to its age is strongly recommended. To achieve this goal it is perhaps possible to use the contained shale and palynomorphs in addition to isotopic age dating on the glauconite present in the formation.

REFERENCES

Barr, F.T. 1972. Cretaceous biostratigraphy and planktonic foraminifera of Libya. *Micropaleontology*, **18**, 1-46.

Barr, F.T. and Weegar, A.A. 1972. *Stratigraphic Nomenclature of the Sirte Basin, Libya.* Petrol. Explor. Soc. Libya.

Ghummed, M.A. 1997. The Satal Formation-Its stratigraphic position, western Sirt Sirt Basin. *In: Geology of the Arab World, 4th Intern. Conf., Cairo.*

Sughair, A.M. 1992. Geochemical investigation of the Bahi Formation in the western part of the Sirt Basin, Libya. *Petrol. Research J.*, **4**, 33-45.